Morpho-tectonics of transpressional systems: insights from analog modeling

Ethan M. Conrad[1,2], Riccardo Reitano[3], Claudio Faccenna[3,4], and Thorsten W. Becker[1,2,5]

[1]Institute for Geophysics, Jackson School of Geosciences, The University of Texas at Austin, Austin, TX, USA.

[2]Department of Geological Sciences, Jackson School of Geosciences, The University of Texas at Austin, Austin, TX, USA.

[3]Dipartimento Scienze Geologiche, Universitá Roma TRE, 00146 Rome, IT..

[4]GFZ German Research Centre for Geosciences Wissenschaftpark "Albert Einstein", Telegrafenberg, 14473 Potsdam, DE.

[5]Oden Institute for Computational Engineering & Sciences, The University of Texas at Austin, Austin, TX, USA

Corresponding author: Ethan M. Conrad (econrad@utexas.edu)

Key Points:

- Feedback between fault and drainage network development regulates the deformation, exhumation, and morphology of transpressional systems
- The progression from distributed deformation to full strike-slip strain partitioning is accelerated in more erosive systems
- Exhumation in a transpressional wedge is maximized along the master fault and axial valley due to heightened rock uplift and incision

Abstract

Transpressional margins are widespread, and their dynamics are relevant for plate boundary evolution globally. Though transpressional orogen evolution involves a topographic response to deformation, many studies focus only on the structural development of the system ignoring surface processes. Here, we present a new set of analog models constructed to investigate how tectonic and surface processes interact at transpressive plate boundaries and shape topography. Experiments are conducted by deforming a previously benchmarked crustal analog material in a meter-scale plexiglass box while controlling erosion through misting nozzles mounted along the transpressional wedge. We used a laser scanner to generate digital elevation models throughout the model evolution and photos for particle image velocimetry analysis. We focus on three experiments that cover a range of rainfall and convergence settings, with two end-member erosion settings and a dry reference. In all experiments, a bivergent wedge forms, and strain partitioning broadly evolves according to previously established models. Regarding drainage networks, we find that the streams in our models develop differently through feedback between fault development and drainage rearrangement processes. Differences between end-member erosional models can be explained by the varying response of streams to structure modulated by rainfall. Additionally, erosion may influence the structural evolution of transpressional topography, leading to accelerated strike-slip partitioning. From these results, we create a model for developing structures, streams, and topography where incision and valley formation along main structures localize exhumation. We apply insights from the models to natural transpressional systems, including the Transverse Ranges, CA., and the Venezuelan Andes.

1. Introduction

Coupling between tectonics and surface processes may affect the localization of deformation and morphological evolution of orogenic systems (e.g., Burbank & Anderson, 2011; Graveleau et al., 2015; Koons, 1995; Molnar & England, 1990; Willett, 1999). When orogenesis is accompanied by a degree of obliquity, the resultant deformation is termed transpression, describing the pairing of wrenching and thrusting structures to accommodate strain (Sanderson & Marchini, 1984). In natural transpressional systems, tectonic strain may be partitioned so that a single vertical strike-slip fault or pairs of strike-slip faults oriented sub-parallel to the zone boundary accommodate the wrench component of oblique convergence (Teyssier et al., 1995). Since most plate boundaries are oblique (> 10º obliquity; Philippon & Corti, 2016), understanding the erosion-tectonic feedback and its relationship with strain partitioning in such settings is essential to accurately constrain, interpret, and model the evolution of the crust and surface.

Recent field observations from transpressional settings suggest that climatic variability may affect deformation patterns, exhumation, and topographic change around major faults (Cochran et al., 2017; Cruz et al., 2007). The stream network response to such change may also vary depending on precipitation and bedrock erodibility (Reitman et al., 2022). Generally, faults control drainage geometries through entrainment (Chorley et al., 1984; Koons, 1994, 1995) and preferential incision by mechanical weakening (Koons, 1994, 1995). These mechanisms are important in orogenic systems since fluvial incision is a primary driver of mass transfer. However, a general understanding of how stream networks and fault structure modify the morphotectonic evolution of a transpressional wedge remains to be established.

"Erosion-tectonic" sandbox models provide valuable insight into transpressional systems by combining tectonic deformation and surface mass transport using appropriate analog materials and misting systems that realistically simulate the erosional processes acting on a deforming wedge (Guerit et al., 2016; Guerit et al., 2018). Previous erosion-tectonic models have been used to study the passive rotational response of drainages to oblique convergence (Guerit et al., 2016) and the transient nature of landscapes under transpression (Guerit et al., 2018). Observations from these studies show that streams have a predictable response to deformation in the absence of confounding variables and can be used to characterize deformation in an oblique wedge. Furthermore, analog models by Malavieille et al. (2021) showed that mass transfer by erosional processes could influence the location of major faults, the topographic response to internal deformation partitioning, and, therefore, the long-term evolution of the wedge.

Here, we present erosion tectonic sandbox experiments that investigate the relationships between fault structure, stream networks, and the strain field in transpressional systems. We attempt to identify the potential feedback between these components to explain morphological and deformational differences between experimental wedges for high- and low-erosion endmembers. Through analyses of digital elevation models and velocity fields from particle tracking, we address 1) how stream networks evolve in transpressional systems under variable erosional conditions, 2) if and how erosion influences the structural and morphological evolution of transpressional mountain belts, and 3), how strain partitioning evolves and is affected by structural and stream network development. The components of wedge evolution related to these questions are highlighted in Figure 1. We extend our results and analyses to natural transpressional prototypes,

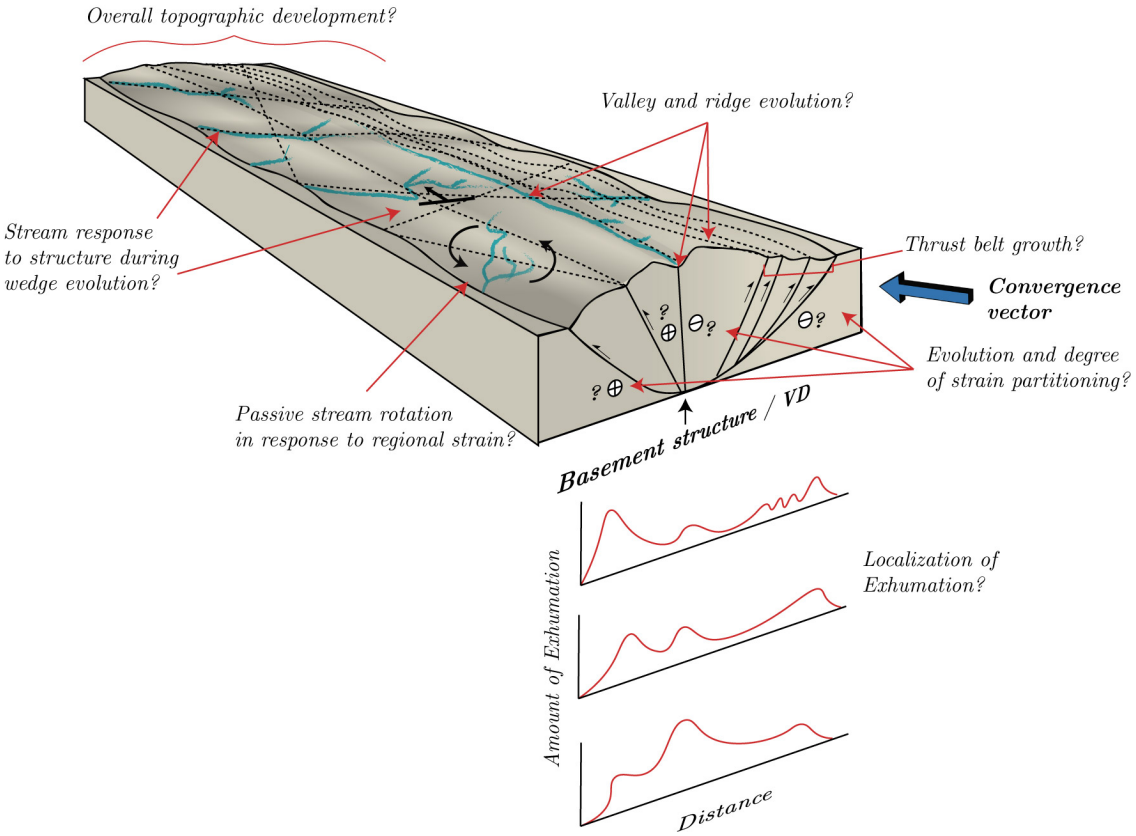

Figure 1. *Illustration highlighting the unresolved components of the growth of a transpressional (left-lateral) wedge addressed in this paper. The velocity discontinuity (VD) and convergence vector are in bold font, dashed lines on topography show fault traces. The* x-y *plots show hypothetical exhumation patterns (red lines) across the wedge. Examples of stream responses to structure shown include drainage deflection (black arrow showing offset), headward erosion, and entrainment along faults. Black rotation arrows indicate the direction of rotation in a left-lateral transpressional orogen.*

mainly focusing on the Merida Andes of Venezuela and the central Transverse Ranges along the San Andreas fault system in California, U.S.

2. Analog model: Erosion–tectonics sandbox

Previous analog studies of the evolution of transpressional mountain belts focus on the structural development of the model without including surface processes (e.g., Barcos et al., 2016; Lallemand et al., 1994; Leever et al., 2011a; Leever et al., 2011b; Pinet & Cobbold, 1992). Some workers have conducted laboratory studies that included the effects of erosion and sedimentation by removing and applying material by hand (e.g., Bonnet et al., 2007, 2008; Konstantinovskaia & Malavieille, 2005; J. Malavieille et al., 1993; Perrin et al., 2013). However, this approach limits the internal control of the system. Only a few models combine tectonic stresses and surface processes using misting systems that more realistically simulate the erosional processes acting on a deforming wedge (Graveleau et al., 2015; Graveleau & Dominguez, 2008; Guerit et al., 2016, 2018; Lague et al., 2003; Mao et al., 2021; Reitano et al., 2022; Viaplana-Muzas et al., 2015, 2019). These “erosion–tectonic” laboratory studies are often limited to purely compressional or extensional settings with few strike-slip (e.g., Graveleau et al., 2015) or transpressional (e.g., Guerit et al., 2016; Guerit et al., 2018) investigations. In the presented experiments, we add to the

current collection of erosion-tectonic studies of transpression and aim to understand how deformation and wedge morphology evolve under the influence of structural and fluvial mechanisms in different erosional regimes.

2.1 Experimental material

Analog materials used in erosion-tectonic experiments should account for the first-order deformational and erosional behavior of the lithosphere (e.g., Graveleau et al., 2011). In addition, the material should scale appropriately, demonstrating geometric, kinematic, and dynamic similarity (Hubbert, 1951). Many granular single component (e.g., crushed quartz, silica powder) and composite materials (e.g., Mat IV or CM2) have been tested and shown to behave similarly to natural cases in a variety of geodynamic experiments (Graveleau et al., 2011). Our material, CM2, is a combination of 40 wt. % glass microspheres, 40 wt. % silica powder, and 20 wt. % PVC powder (Reitano et al., 2020). Reitano et al. (2020) characterized CM2 following the work of Graveleau et al. (2011), who developed a similar material, Mat IV. Mat IV has the same composition as CM2, yet 2 wt. % graphite powder and 18 wt. % PVC. These authors show that CM2 and Mat IV deform following the Mohr-Coulomb failure criterion, exhibit natural basin and channel characteristics, and appropriately balance hillslope diffusion and channel incision. They are also velocity-weakening materials leading to stick-slip. Since Reitano et al. (2020) only report the hydrated frictional behavior (20 wt. % H_2O) of CM2, we conduct rotary shear tests to characterize its dry frictional behavior. These tests were conducted using an energy controlled rotary shear apparatus (see Conrad et al., 2023) fitted with a granular sample holder (Conrad et al., 2020).

2.2 Experimental setup

We conduct experiments in a 2 m × 1 m × 0.5 m plexiglass box, with ends left open for drainage (Figure 2a). The basal slope is fixed at 1º to ensure water exits the system. We set a mylar sheet inside the box and fix a plexiglass board cut to the desired obliquity to the sidewall. By pulling the mylar sheet beneath the board, we simulate oblique convergence (Figure 2b). We load the board–sheet set up with a ~5 cm thick package of the experimental material hydrated to ~20 wt. % water (see section 2.1). The length and width of the material package are controlled to ensure that the edges do not influence the wedge's evolution or reach the sidewalls of the box. Free boundaries are particularly important on the fixed side of the model as it allows the wedge to form independent of the geometry of a rigid backstop (e.g., Guerit et al., 2016). This independence arises because the material properties, rather than the backstop dip, control the geometry of the wedge. Additionally, the thrust can propagate beyond the location of a would-be backstop.

We use the velocity discontinuity (VD) between the fixed board and moving sheet to localize deformation, forming a bivergent wedge in the material package. This approach is similar to Leever et al. (2011a,b) and the classic wrench experiments of (Riedel, 1929), where the VD simulates a basement fault beneath a homogenous sediment cover. We initiate surface processes using misting nozzles mounted on an aluminum crossbar aligned with the wedge trend. These nozzles maintain a droplet size of fewer than 100 μm to avoid rain splash erosion (Bonnet et al., 2007; Graveleau et al., 2012; Lague et al., 2003; Reitano et al., 2022; Viaplana-Muzas et al., 2015, 2019).

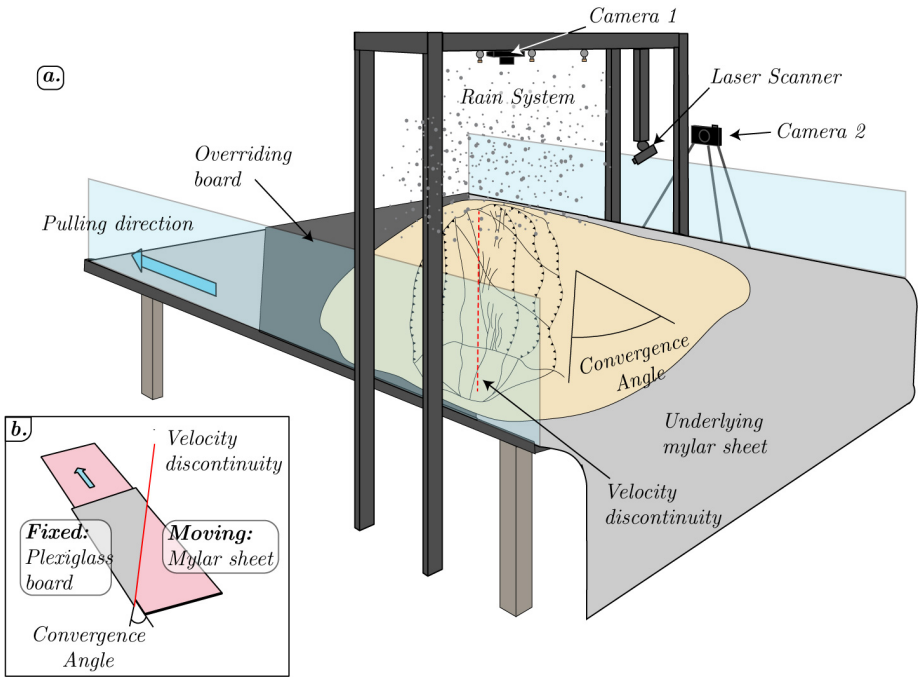

Figure 2. (a) *Cartoon showing the experimental set-up. The experiment is comprised of a 2 × 1 × 1 m plexiglass box set on a tabletop. The beige feature represents the material loaded on top. The red line shows the velocity discontinuity and the blue arrow on the left is the pulling direction. The motor that pulls the mylar sheet is not pictured.* ***(b)*** *The velocity discontinuity set-up that was put into the box to generate a deformational wedge. The gray color represents the plexiglass board cut to the desired convergence angle. The pink represents the mylar sheet that was pulled under the board. The velocity discontinuity (red line) is the interface between the fixed and moving materials.*

2.3 Parameters varied

We selected three representative experiments (bold font in Table 1) out of ten that explored a more extensive range of rainfall and convergence settings. These additional experiments test the model sensitivity, ensure reproducibility, and explore the parameter space. Most experiments were performed with a convergence angle of 20º to investigate wrench-dominated transpression (see Teyssier et al., 1995). For comparison, we conducted one model at 40º. Convergence rates ranged from 65 to 325 mm hr^{-1}, and rainfall rates from 0 to 26 mm hr^{-1}. The three presented experiments provide the most robust and comparable datasets considering the scope of this paper: "dry" (D_62422), "low erosion" (W_71322), and "high erosion" (W_62722). The prefixes D and W are for dry and wet experiments and the suffix is the date experiments were conducted. In the table, the CR refers to a dimensionless quantity defined as the convergence over rainfall rate (Reitano et al., 2022). An infinite CR means the system is completely dry, whereas a CR of 0 indicates the system is tectonically quiescent. We present these tests as representative "wet" ("low" and "high erosion") and "dry" CR scenarios at a convergence angle of 20º. Due to the highly differing boundary conditions between a completely dry experiment and one subject to consistent misting, the wet experiments are more directly comparable.

We consider results robust if fault geometries and the dimensions and general shape of the wedge are reproducible between models. Furthermore, we ensured that throughout the main stages, there was no connectivity between drainages propagating from the edge of the model and drainages within the wedge. The latter is necessary because the edge drainages provide a lower base level.

Table 1. *All experiments conducted using the sandbox set-up. Prefixes D and W denote wet and dry experiments, respectively. The CR is the ratio between convergence and rainfall rates.*

Experiment #	Convergence Angle (º)	Convergence rate (mm/hr)	1σ	Rainfall rate (mm/hr)	1σ	CR	Refered to in text as:
D_62422	**20**	**320**	**40**			**Inf.**	**"Dry"**
W_62321	20	240	9	20	6	12	
W_62421	20	80	6	15	4	5	
W_71321	**20**	**230**	**11**	**31**	**13**	**7**	**"Low erosion"**
W_70221	20	80	14	26	11	3	
W_71521	40	70	11	26	11	3	
W_62722	**20**	**70**	**24**	**34**	**11**	**2**	**"High erosion"**

Therefore, once connected with the wedge network, these outlets would localize and increase the erosion mass flux out of the wedge, dominating the topography and drainage network morphology (Leopold & Bull, 1979).

2.4 Scaling

To dynamically scale experiments to natural systems, we should follow the principles outlined by Hubbert (1937) and Ramberg (1981). However, given uncertainties about the physics of surface transport, it is not entirely clear how to upscale surface processes. We follow previous work by considering kinematic similarity only rather than dynamic scaling. This approach might be appropriate if erosional processes are scale-invariant (Sapozhnikov & Foufoula-Georgiou, 1996), leading to potential scale independence (see Paola et al., 2009, for discussion). In terms of geometric comparison with nature, we define a length scaling factor, $l^* = l_{model}/l_{nature}$. Given the approximate dimensions of transpressional mountain belts (l = ~10^5 m, w = ~10^4 m) and that of the wedges generated in the experiment (l = 1 m, w = 10^{-1} m), $l^* = 10^{-5}$, meaning 1 cm in the model represents 1 km in nature. To derive the time scaling factor, t^*, we use the erosion number scaling approach of Reitano et al. (2022) to estimate $t^* = 4 \times 10^{-11} – 4 \times 10^{-10}$. These values suggest that 1 hour of model time corresponds to 300 kyr – 3 Ma, as in prior work (Graveleau et al., 2011; Mao et al., 2021; Reitano et al., 2022). This scaling approach assumes that material accreted to the wedge is balanced by material removed by erosion. In this case, the difference in material erodibility, k, between model and nature can be evaluated as $k^* = v^*/4l^*$, where v^* is the convergence rate scaling factor ($v^* = 10^4$-10^5). Using this v^* and the l^* found above, k^* is between 10^9-10^{10}.

2.5 Analysis

We monitor the structural and surficial evolution by scanning the model incrementally with a laser scanner to create digital elevation models (DEMs) and conducting particle image velocimetry (PIV) from photos taken every minute. Vertical and horizontal resolutions for the laser are 0.07 mm and 0.05 mm, respectively. Scans are taken at 10 cm, 15 cm, 25 cm, and 35 cm of convergence. We chose the first increment based on our preliminary experiments, where we determined that this much convergence creates sufficient relief (~1 cm) for realistic drainages to develop. The subsequent increases provide 10 cm increments (+30% shortening) of experiment evolution up to a maximum of 35 cm (considered 100% shortening). These stages are appropriate

given spatiotemporal constraints, including the influence of edge effects, which grow with rain time and total displacement. After this amount of shortening, especially for high rainfall experiments, the influence of drainages and faults propagating from the boundary cannot be neglected. We use the MATLAB software TopoToolbox (Schwanghart & Scherler, 2014) to analyze DEMs and the corresponding stream networks across the experimental stages. Structural interpretations are made of each stage by pairing DEMs with photographs, which more clearly display structures lacking sufficient vertical offset to be resolved by the laser scanner.

We derive the evolution of the velocity field using a 2-D cross-correlation technique, Particle Image Velocimetry (PIV, see Raffel et al., 2007), with the MATLAB toolbox PIVlab (Thielicke & Sonntag, 2021). However, there are some unavoidable limitations and high amounts of noise associated with using this technique in the presence of a rain system, as surface transport is also partially tracked, and mist affects the quality of the images. Yet, with a 1-minute capture rate, image pre-processing, and velocity filtering, PIV can provide insight into the differences between end member erosional cases. We preprocess images using a contrast-limited, adaptive-histogram equalization filter and auto-contrast stretch. To generate velocity fields, we use a Fast Fourier Transform PIV algorithm across a region of interest of 2253×784 px with an initial interrogation area of 116 px, and three passes down to 32 px, and a gauss 2×3 point sub-pixel estimator (see Thielicke & Sonntag, 2021). Resultant velocity fields were calibrated using a photo reference and analyzed and plotted using Generic Mapping Tools (Wessel et al., 2019). We calculate the horizontal component of the velocity, u, the maximum horizontal shear strain rates, $\dot{\varepsilon}_s$, and the dilatational strain rate, $\dot{\varepsilon}_m$. The strain components $\dot{\varepsilon}_s$ and $\dot{\varepsilon}_m$ allow us to analyze the localization of strike-slip and compressional/extensional deformation, respectively. For ease of comparison between frames of each experiment, we normalize the values by the standard deviation in each frame and denote the normalized u, $\dot{\varepsilon}_s$, and $\dot{\varepsilon}_m$ as $\hat{u}$, $\hat{\dot{\varepsilon}}_s$, and $\hat{\dot{\varepsilon}}_m$, respectively.

3 Results

3.1 Structural evolution

Figure 3a shows the DEM results of the three presented experiments (dry, low erosion, high erosion), and Figure 3b shows the interpreted structural evolution of all models. For reference we show contrast-enhanced images of the final model stages in Figure 3c-d. To describe our models, we use the wrench fault terminology of Naylor et al. (1986). Fault progression begins with the appearance of *en-echelon* synthetic shears (*R*, 15º – 30º) that initiate sub-parallel with the convergence direction and delineate rhomboidal packages within the wedge. Within the viewing frames, these features form at least three clear packages, which can be directly compared between models. *R*-shears are accompanied by antithetic shears (*R'*, 65º - 90º) and connecting splays (*S, >17º*). The left-lateral displacement of material packages initiates the main inboard (on the fixed side of the model) thrust (bottommost thrust in Figure 3b), followed by the formation of an outboard (on the moving side of the model) back-thrust. Together these features form "*pop-up"* structures, which accommodate the uplift of the blocks. While somewhat obscure in erosional models due to erosion/sedimentation, a notable low-angle shear striking in the opposite direction (*P, 180º - 165º*) forms in all models outlining the bottom-left portion of an elongate diamond-shaped or *"pug-nosed"* landform (Figure 3a).

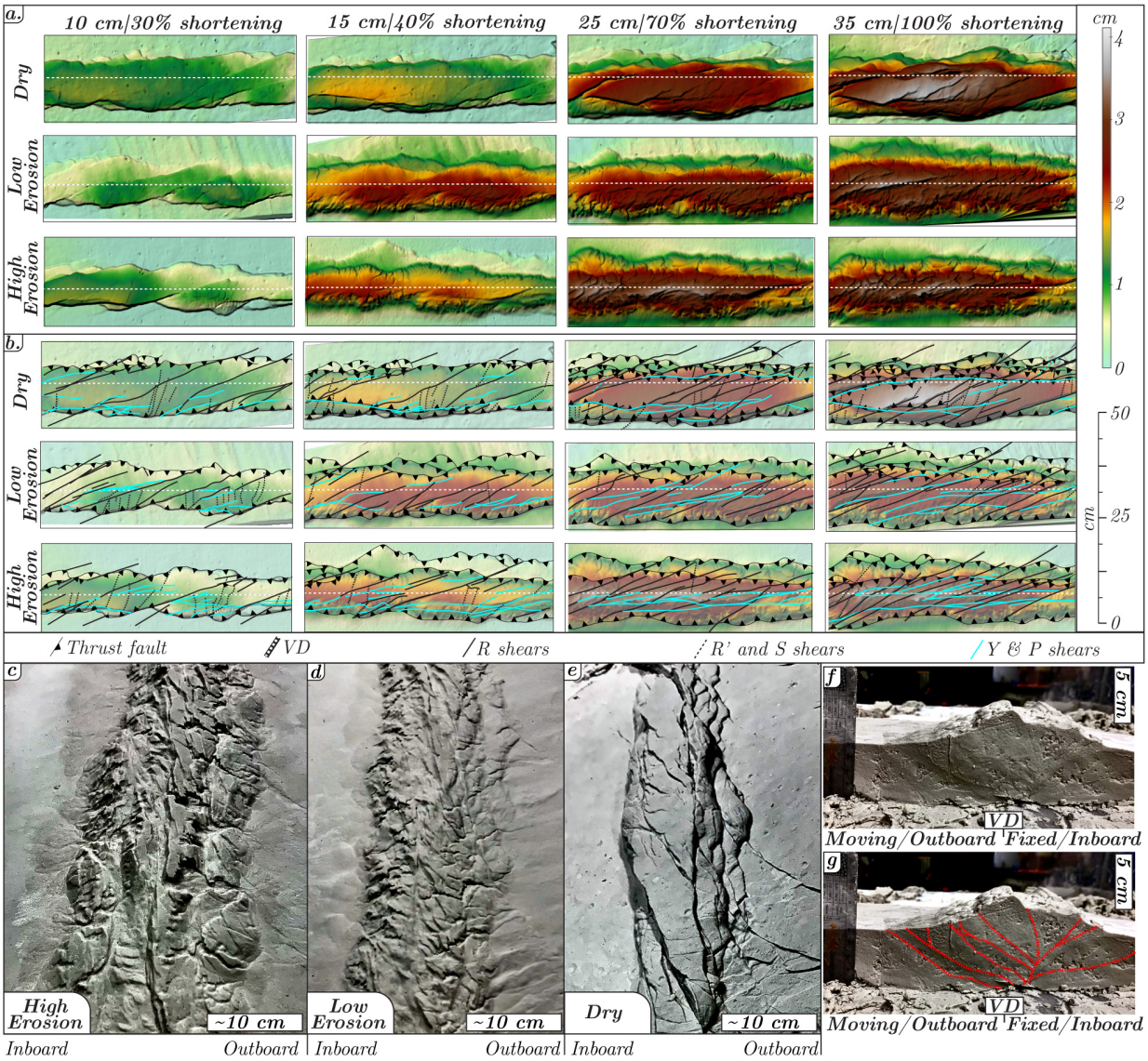

Figure 3: *Overview of the results of selected experiments.* ***(a)*** *Digital elevation models (DEMs) across shortening stages. Rows show increasing erosion and columns show increasing convergence/shortening. White lines represent the location of the velocity discontinuity (VD).* ***(b)*** *Interpreted structures showing thrusts (decorated lines), the VD (white dashed line), riedel (R) shears and connecting splay (S) faults (black lines), anti-riedel (R') shears (dotted black lines), and low-angle faults (Y- and P-shears, see text for description, cyan lines).* ***(c-e)*** *Contrast enhanced oblique images at the final stage of each model. Scale bars are only accurate at the bottom of the images due to perspective distortion. Note the alluvial fans in the erosion models* ***(c,d)****.* ***(f-g)*** *Contrast enhanced images showing the uninterpreted* ***(f)*** *and* ***(g)*** *interpreted cross sections of the high erosion model.*

The main inboard thrust feature moves only a few centimeters during the evolution of each model (2.3 cm, 3.4 cm, and 3.3 cm for dry, low erosion, and high erosion models, respectively). The outboard thrust belt propagates throughout the model at distances depending on the presence/amount of erosion. Thrust sheets nucleate at the tips of the *R*-shears that extend into the undeformed inboard and outboard sections of the model. With further convergence, lower angle *R*-shears (*Y*, 0º - 15º) form and coalesce with *P*-shears into an anastomosing VD-parallel master

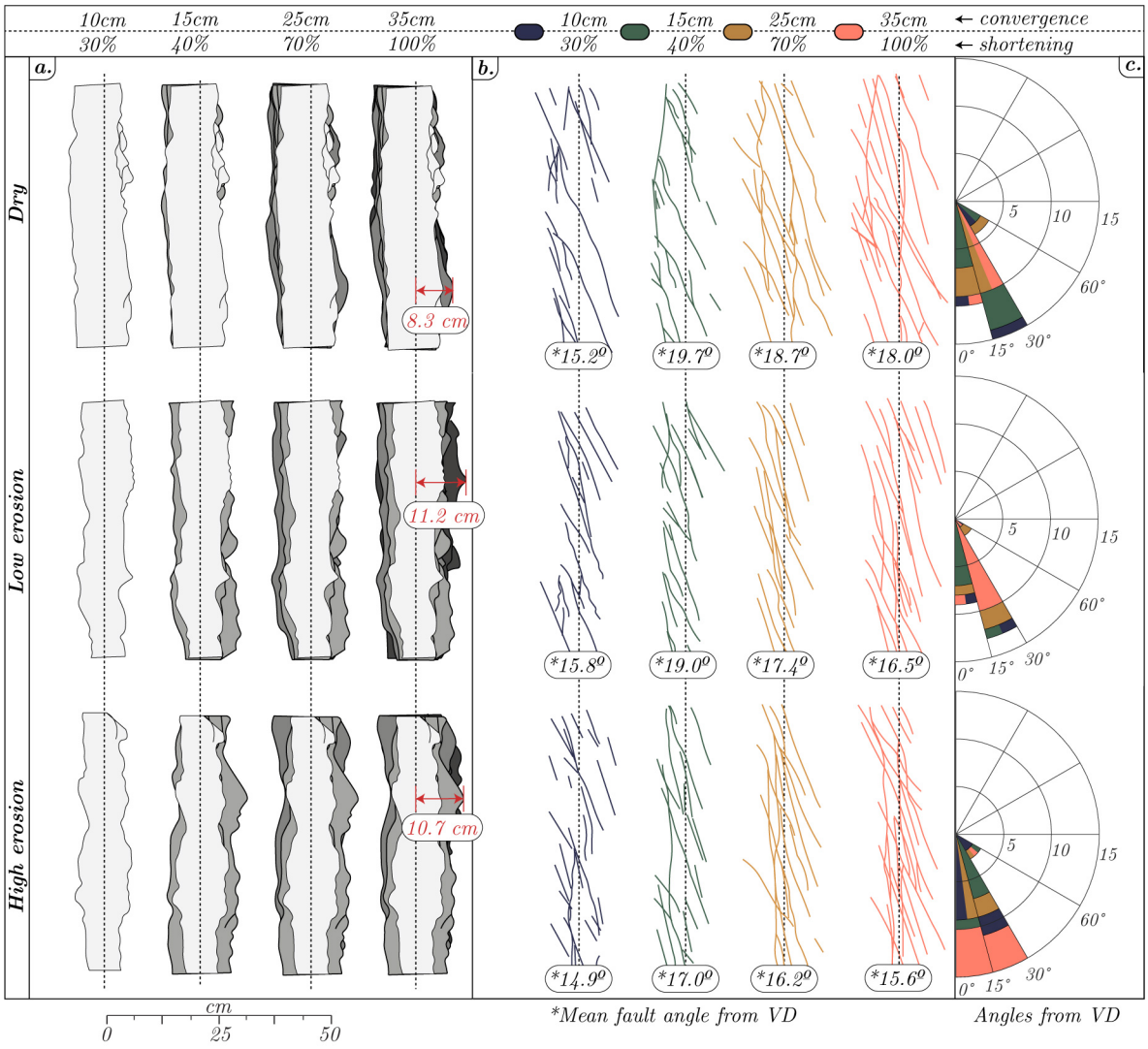

Figure 4: *The evolution of thrust sheets and internal strike-slip faults with increasing shortening. The upper, middle, and lower rows show the dry, low erosion, and high erosion models, respectively.* ***(a)*** *Change in thrust belts with increasing convergence. Each grey shade represents a horizontal slice through the wedge. These slices are stacked at each convergence step. The horizontal black dashed lines are the velocity discontinuity.* ***(b)*** *The evolving internal strike-slip structure of the models.* ***(c)*** *Polar histograms showing the number of structures within 15° bins from 0 to 60°. Colors in the histograms correspond to the convergence stages as shown at the top of the figure. Split bins represent subsequent stages with no change in count. Faults and fractures > 60° and < 0° were included in those nearest bins, because they are uncommon and deviate only small amounts from those angles.*

fault zone. In some cases, *R'* oriented fractures accommodate an extensional component. In either case, these fractures have an apparent clockwise rotation as they are offset by the left lateral *R*-shear system. *R*-shears may have an extensional component after they no longer accommodate strike-slip motion, especially when they optimally intersect with the evolving master fault and develop a releasing bend. This occurrence is prevalent in the later stages of the model. *R*-shears also tend to form arcs concaving into the VD and sometimes form sharp cusps at the VD-fault intersections (Figure 3b). Overall, the structural evolution of the experiments agrees with what is described by prior analog studies of wrench-dominated fault zones (e.g., Casas et al., 2001; Cloos,

1928; Leever et al., 2011a,b; Naylor et al., 1986; Pinet & Cobbold, 1992; Riedel, 1929; Schreurs & Colletta, 1998, 2002; Tchalenko, 1968; Wilcox et al., 1973). Though challenging to interpret, as the material is monochromatic, high-contrast photos of cross sections cut through the high erosion model (Figure 3f,g) show the complex internal deformation within the wedge, interpreted as a thrust-bounded, upward tulip shaped structure (Figure 3g).

To compare the evolution of thrust faults across the models, we show superimposed horizontal topographic slices for each model and stage (Figure 4a). From dry to high erosion, the number of thrust sheets increases at each time stage yet are narrower, forming distinct half-moon-shaped salients. Contrary to the other models, the first thrust sheet that initiates in the high erosion model remains dominant for most of the experiment. This sheet is nearly as wide as the maximum extent of the thrust sheet in the low erosion model and exceeds that of the dry model (3.3 cm). Subsequent thrust initiation in the low erosion model eventually overtakes that of the high erosion model. The maximum thrust toe distance from the VD across all stages is 8.3 cm, 11.2 cm, and 10.7 cm for the dry, low, and high erosion experiments, respectively. Thus, the drier systems initiate more yet thinner thrust sheets but still achieve nearly equal or greater cumulative widths at 17 cm, 21 cm, and 16 cm, respectively.

There are evident changes in the evolution of the intrawedge strike-slip faults between experiments. We illustrate this in Figures 4b and 4c by extracting the surface traces of these faults, calculating their orientation (Figure 4b), and binning them into rose diagrams (Figure 4c). Dry models show a slight change in the geometry of shears through each stage, with a subtle indication of the eventual through-going, master wrench-fault formation. This final-stage fault seems to reactivate the initial outboard thrust fault plane. Conversely, erosion models show a more significant change in intrawedge shear geometry and an earlier coalescence of shears into a clear, through-going wrench fault. From inspection of such traces, low-angle faults that begin to merge into the master fault dominate the later stages of the high erosion model. However, faults are more distributed with more *R*-shears for the low erosion and dry experiments. Visualizing this in the rose diagrams (Figure 4c), the high erosion model has more fault traces (n = 15) within 15º of the velocity discontinuity.

3.2 Stream Evolution

Figure 5 shows snapshots of the drainage evolution of the high and low erosion models. After we engaged the rain/mist system, streams nucleated orthogonal to the trace of the thrust sheets (transverse orientation). As convergence continued, streams evolved following various well-described mechanisms: headward erosion, drainage deflection by strike-slip motion, drainage capture, and drainage beheading (see Bishop et al., 1995, for review). From observations of pictures and DEMs, it is apparent that faults strongly control the initiation of streams and pathways of headward erosion. As a result, we generally observe asymmetric forked to rectangular drainage patterns with consistent spacing and sharp angles defining tributary junctions.

Streams that initiate in the *R-shear* direction erode headward throughout the evolution of the model and follow the reorientation of *R-shear*s described above. With the left-lateral deflection of transverse drainages along *R-shear*s, these '*R*-streams' are captured, resulting in sharp cusps in the drainage topology. This pattern is apparent on both the main thrust and thrust belt sides of the wedge. However, on the main thrust portion, transverse streams dominate the evolving networks. In both models, major valleys capture the flow of several transverse streams following the *R*-shear

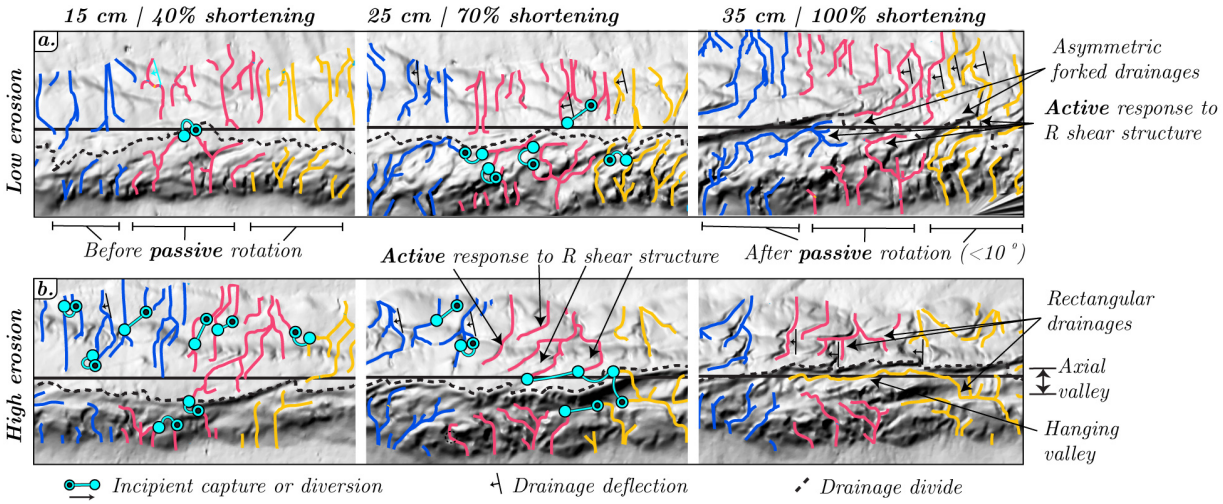

Figure 5: *Snapshots of stream evolution between erosion models. Streams are cut to the lowest thrust sheet and colored as a visual aid to tracking reorganization mechanisms between frames.* ***(a)*** *Low erosion model. The active drainage response to structure is more delayed, while the passive rotation is better expressed (preserved). Drainages networks exhibit asymmetric forked patterns in the final stage.* ***(b)*** *CR2 model. The active drainage response to structure occurs earlier, yet there is a less apparent passive rotation response. Final drainage patterns are rectangular in form.*

structures in the low erosion model and the VD-parallel master fault in the high erosion model. The capture of this valley by transverse tributary drainages causes punctuated erosion events.

In the high erosion model (Figure 5b), the primary drainage system shows less branching and is more aligned with the velocity discontinuity. Furthermore, *R*-streams initiate early and are more rapidly captured by transverse streams, resulting in more rectangular drainage networks with sharper junctions. Similarly, captures are less prevalent in the low erosion model - with one capture pair (linked blue dots) compared to eight in the high erosion model at 40% shortening (Figure 5a). As a result, faults more consistently entrain streams in the direction of structures forming forked asymmetric drainages. Lastly, as described in section 4.2, the intersection of *R*-shears with the master fault may form a releasing bend, expressed geomorphologically as a partially restricted lofted valley in our high erosion system.

3.3 PIV analysis of velocities and strain-rates

From the normalized velocities, $\hat{u}$ (Figure 6a) and strain-rates, $\hat{\dot{\varepsilon}}_s$ (Figure 6b), and $\hat{\dot{\varepsilon}}_m$ (Figure 6c) derived through our PIV analysis, we recognize three main phases of strain-rate field evolution common for all models. In Figure 6d, we extract the structures corresponding to sharp gradients in $\hat{u}$ (Figure 6a) and related bands of high $\hat{\dot{\varepsilon}}_s$ (Figure 6a). Velocities are particularly useful in verifying shear zones and differentiating them from noise imposed by landsliding or mist interference (red blobs in Figure 6a).

Some early organization phases occur before the first panel in Figure 6, beginning with distributed deformation followed by shear strain localization along *R* faults at 6-9% shortening (not pictured). Before the first frame in Figure 6, there is also a stage of distributed deformation and shear strain localization on *R*-faults (stage 1 in Figure 6). Shortly after, elevated $\hat{\dot{\varepsilon}}_s$ values are focused on the sides of the wedge (10 cm convergence / 30 % shortening), marking a phase of incomplete partitioning and oblique faulting on the major thrust structures (stage 2 in Figure 6).

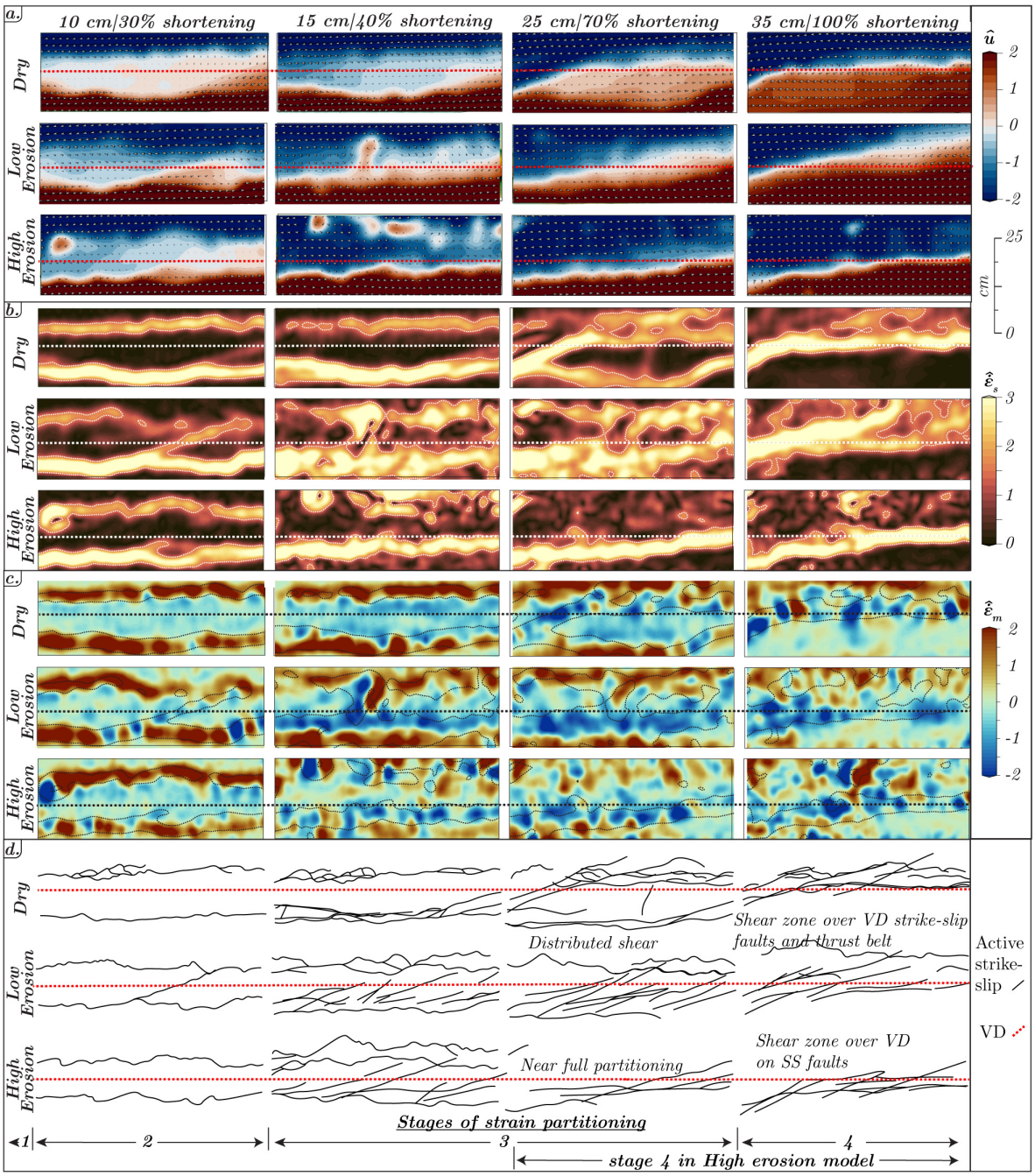

Figure 6: *Evolution of strain partitioning from PIV at the same stages shown in Figures 2, 3, and 4.* ***(a)*** *The normalized horizontal velocity components ($\hat{u}$). Sharp color contrast indicates locations of strike-slip deformation. Irregular red blobs show locations of land sliding or noise caused by mist interference. The dashed red line indicates the velocity discontinuity (VD).* ***(b)*** *The normalized maximum horizontal shear strain-rate at each stage ($\hat{\varepsilon}_s$). White dotted lines are superimposed $\hat{\varepsilon}_s = 1.5$ contours. The dashed white line indicates the VD.* ***(c)*** *The normalized dilatational strain-rate, ($\hat{\varepsilon}_m$). Positive values (red) indicate compression, negative values (blue) indicate extension. Black dotted lines are superimposed $\hat{\varepsilon}_s = 1.5$ contours. The dashed black line indicates the VD.* ***(d)*** *Active faults determined by interpreting fault locations with respect to $\hat{u}$ and $\hat{\varepsilon}_s$. The dashed red line indicates the VD. The evolution is broken into four stages of strain partitioning: 1) distributed strain and en-echelon R-shear formation, 2) oblique slip on bivergent thrusts, 3) transitional strain partitioning, 4) full partitioning to throughgoing structure (s).*

314

The experiments then enter a transitional stage (stage 3 in Figure 6). Synchronous with the structural evolution, strike-slip motion becomes increasingly localized on a narrow band of anastomosing strike-slip faults (Figure 6c). The high erosion experiment achieves near-complete strike-slip strain partitioning at 70% shortening (stage 4 in Figure 6). For the other experiments, complete strike-slip partitioning does not occur until the final frame (35 cm | 100% shortening) at the earliest (i.e., if the model continues, the evolution likely progresses). This difference suggests that the strain partitioning evolution is accelerated in the high erosion model. The more prevalent noise from land sliding attests to more vigorous sediment routing out of the wedge. Balanced by compression at the boundaries, the interior of the wedge is under extension in each model and stage (Figure 6c). This band becomes localized to the master-fault zone as the models progress and compression becomes less organized. Additionally, more restraining bends (red anomalies in blue extensional bands) occur along the master-fault zone in the dry model compared to wet models.

3.4 Topographic evolution

Initial topography forms along pop-up structures as rhomboidal slices (Figure 3). With the onset of thrust belt propagation, the topography develops transverse asymmetry, with one steep side corresponding to the main thrust and a broader side corresponding to the thrust belt. As can be seen from the differences between the dry and erosion models, hillslope diffusion and stream erosion drastically modify the topography by incising valleys and causing fault scarps to retreat inward toward the velocity discontinuity. Alluvial fans fill the recessed portions of ridges. As expected, there are broader and higher volume alluvial fans and more deeply incised channels in the high erosion model (Figure 3c-e). In the dry model, the final topography resembles an uplifted and broadly concave plateau. With increased erosion, the topography is more rugged and characterized by steeper peaks and more incised valleys.

Figure 7a shows the changing width of the wedges. The high erosion model shows an increase in width of >5 cm after the first erosional stage, then a plateau with continued convergence. On the other hand, the low erosion model width shows a slightly smaller increase, approximately 4 cm, yet continues to grow as the experiment continues. The dry model has a broader initial topography and shows slow and steady growth in the wedge width from 14 to 15.8 cm. As the experiment evolves, it is marked by a higher curvature thrust belt and more salients and recesses. Furthermore, there is no channel incision, resulting in a broad wedge dissected only by strike-slip structures. The characteristic diamond or *"pug-nose"* shape of wrench-dominated systems is most evident in the dry model due to the intersection of *P* and *R-shear*s (Figure 3a). With increased erosion, structures that do not accommodate significant displacement become less apparent. For instance, in the erosion models, the scarp of the uplifted *P* and *R-shear*s that delineate the diamond structure is eroded in the outboard direction, nearly hiding the feature altogether. There are also differences in relief across strike-slip faults between models. For the high erosion model, *Y* structures have more relief. In the dry and low erosion model, relief is higher on *R* structures.

The surface uplift seems to progress similarly in all models, with only subtle differences in the rate and magnitude. Notably, the high erosion model reaches 3.5 cm earlier at 70% shortening and remains constant until 100% shortening. From 0 to 25 centimeters, each experiment shows an initial phase of more rapid uplift (3 – 3.5 cm at 25 cm of convergence) followed by a slow rise, perhaps approaching a limit of around 4 cm (Figure 7b). Figure 7c shows the elevation of the wedge divided by the distance of the thrust toe from the *VD*. The inverse tangent of the plotted

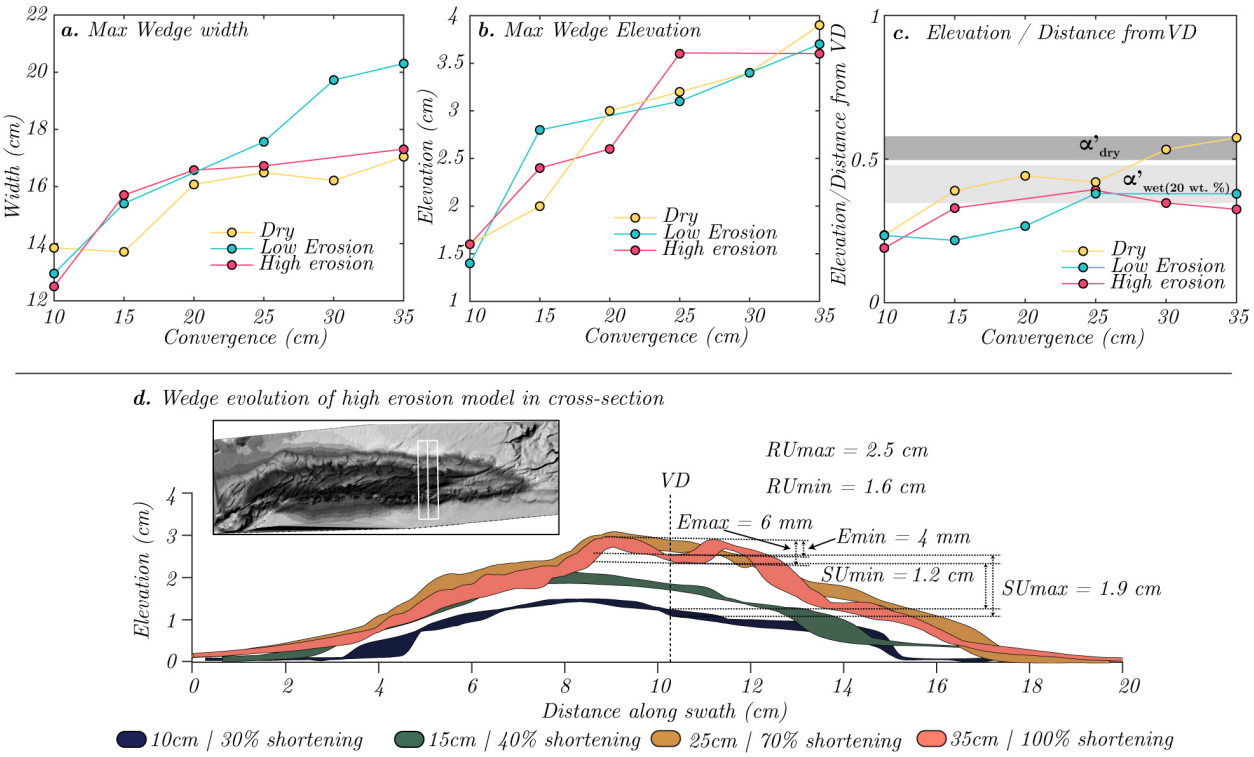

Figure 7*. The topographic evolution of the presented models.* ***(a)*** *Maximum wedge width,* ***(b)*** *elevation, and* ***(c)*** *elevation divided by distance from the velocity discontinuity (VD). The gray bars are the error windows for the theoretical wedge slope calculated from critical taper theory (see Dahlen, 1990) using the material parameters for wet (20 wt. % H_2O) CMII from Reitano et al. (2020), α'_{wet}, and dry CMII (measured), α'_{dry}.* ***(d)*** *Wedge evolution of the high erosion model in cross section with estimates of erosion (E), rock uplift (RU), and surface uplift (SU). The inset shows the location of the swath at the final stage (convergence = 35 cm / shortening = 100%).*

values is effectively the slope of the thrust belt. Using the peak angle of internal friction, ϕ, of wet CMII (ϕ = 25-36, reported in Reitano et al. 2020) and the measured ϕ of dry CMII (ϕ = 44-48) the error window for the inverse tangent of the theoretical dry and wet wedge slope angle, α, from critical taper theory (see Dahlen, 1990) is α_{dry} = 27º - 30º and α_{wet} = 19º – 26º. The tangents of these alpha windows, α', are plotted in Figure 7c (α'_{dry} = 0.53 - 0.57, α_{wet}' = 0.35 – 0.48). Initially, the thrust belt slope in the dry and low erosion models increases into the α_{wet} window, reaching a value of approximately 0.4 at 70% shortening . The wedge slope in the high erosion model slightly decreases at first, corresponding to the propagation of a wide thrust sheet, then similarly increases to 0.4 at 70% shortening. Besides a slight decrease of ~0.05 in the low erosion model, from 70% to 100% shortening, the wedge slope reaches a steady state in the wet models. In contrast, in the dry model, it continues to steepen, nearly exceeding the maximum α_{dry}.

A cross-section of wedge evolution is shown in Figure 7d with corresponding estimates of rock and surface uplift and erosion. The highest rock uplift is located at the VD, which in the high erosion case corresponds with the trend of the axial valley where surface uplift is locally low. Therefore, exhumation is at a maximum at this location.

3. Discussion

4.1 Drainage evolution in response to transpressional tectonics

Considering the experimental results (Figure 5) and the modes of drainage reorganization described in the literature (e.g., Bishop, 1995; Bloom, 1998; Castelltort et al., 2012; Hallet & Molnar, 2001; Koons, 1994, 1995; Ramsey et al., 2007), we group stream response mechanisms to tectonic deformation into two categories:

1. a dynamic reorganization response influenced by the structural evolution of the orogen.
2. a passive response to local strain.

The primary drainage rearrangement mechanisms that enable the dynamic reorganization response to structure are entrainment by fault block growth, diversion and beheading by lateral displacement, and lengthening and capture by headward erosion and preferential fault plane incision (Bloom, 1991; Koons, 1994, 1995; Bishop, 1995). Figure 8a-j shows several examples of these dynamic responses. The evolution of each drainage network can be considered the result of the linear combination of these mechanisms.

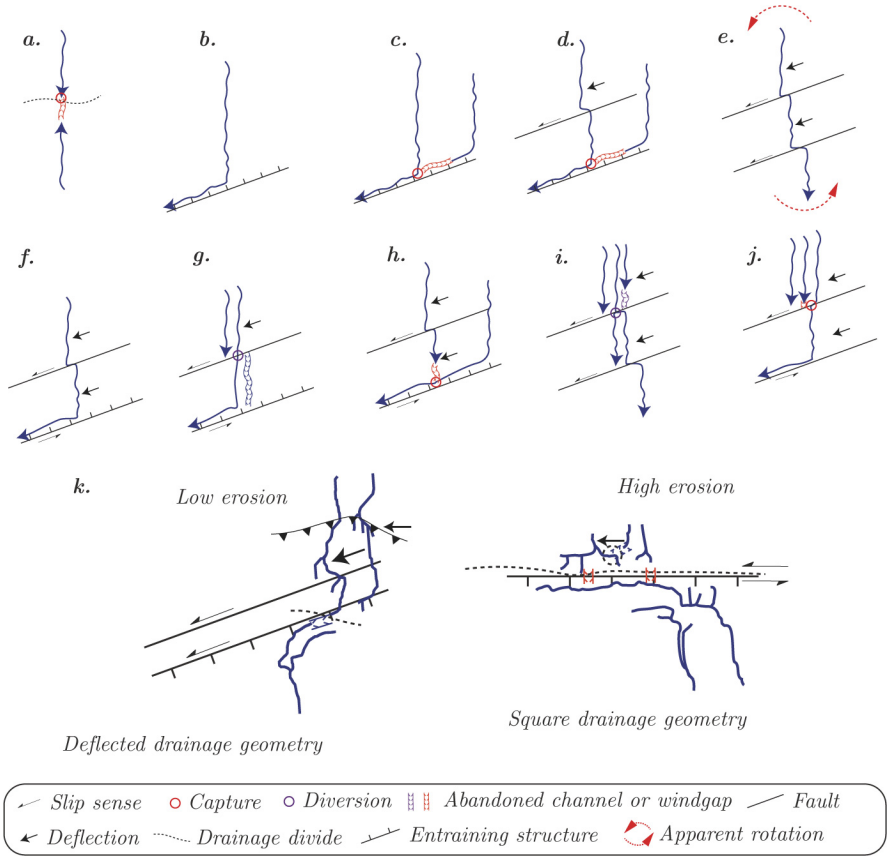

Figure 8: *Examples of drainage reorganization mechanisms leading to the drainage patterns in the high and low erosion models.* ***(a)*** *across divide capture,* ***(b)*** *structural entrainment,* ***(c)*** *structural entrainment and capture upstream along R-shear,* ***(d)*** *deflection, entrainment, and capture upstream along R-shear,* ***(e)*** *deflection,* ***(f)*** *deflection and entrainment,* ***(g)*** *deflection, beheading, diversion, and entrainment,* ***(h)*** *deflection and capture of transverse stream by stream along R-shear,* ***(i)*** *deflection, diversion, and beheading, and* ***(j)*** *deflection, diversion, beheading, and entrainment.* ***(k)*** *shows representative streams extracted from high and low erosion DEMs and thus, how these mechanisms may combine to dictate differences in drainage patterns between models. Clearly, the structural evolution has an impact on the geometry forming more rectangular drainages in the high erosion model.*

Differences in stream network geometry between erosion models suggest that the rate at which the drainage system responds to structure controls the potential feedback with structural evolution (Figure 5). More erosive conditions (headward erosion, capture) favor some dynamic stream response mechanisms and, thus, a shorter response time to structural change. However, other mechanisms, such as deflection and preferential incision, rely on more structurally dominated stream paths (Koons et al., 1994). In Figure 5, drainages in the high erosion model respond more quickly to the structural evolution of the model and deflection in the direction of *R*-shears, with a response evident at 70% shortening. There are also more capture pairs at 40% and 70% shortening, with 12 in the high erosion model compared to 6 in the low erosion model. Due to this heightened response, high erosion stream networks are more rectangular, and a clear axial valley forms with 4-6 mm of incision. Alternatively, streams in the low erosion model have a more delayed response forming asymmetric forked drainage networks in the final stage. To highlight these differences, in Figure 8k, we show single characteristic drainage basin networks from both the high and low erosion models.

The processes described above may explain the formation of a more incised axial valley by drainage redirection in the high erosion model (Figure 5) due to higher strain localization on the master fault (Figure 6b) and pervasive along-strike extension (Figure 6c). The material in these shear zones is weakened by the concentration of mechanical strain and erosional energy along fault damage zones as a function of the strain-weakening behavior of the material (Vermeer & De Borst, 1984). Such strain-weakening behavior was described in the material characterization of Reitano et al. (2020). In both cases, vertical offsets along main structures (1 mm – 10 mm) entrain streams so that they reflect the orientation of the active fault system, especially at later stages once extension becomes concentrated on the master fault, and the stream-structure feedbacks are well-developed.

Once deeply incised, streams may also rotate with the local strain field, described here as the passive response to local strain (Castelltort et al., 2012; Goren et al., 2015; Guerit et al., 2018; Hallet & Molnar, 2001; Ramsey et al., 2007; Zeitler et al., 2001). In both the high and low erosion models, the passive response is less commonly observed but nevertheless tracks the anticlockwise rotation of some blocks up to a few degrees (Figure 5). The stepwise left-lateral deflection of stream segments (Figure 8e) further assists the apparent rotation.

For a stream to be a passive strain marker, the initial orientation of streams should be nearly perpendicular to the trend of the wedge, so they are ideal for rotation with the strain-rate field and can be reliably measured. The initial orientation of such streams seems to be controlled by the *R'* fracture structure. These streams follow the nucleation and rotation of *R'* fractures (< 10º) with continued convergence (Figure 5a). Passive streams must also be in a place where shear strain is distributed equally across their length because shear strain is localized differently depending on the stage of the experiment. Therefore, even with poor fault exposure, streams can provide insight into where shear strain is localized in a wedge and how mature the orogen is regarding the evolution of strike-slip partitioning.

4.2 Links between fault structure, erosion, and the evolution of strain partitioning

In general, the structural and strain partitioning results of our experiments agree with the experiments of Leever et al. (2011a) using a dry quartz sand pack laid upon a velocity discontinuity. Building on the work of Pinet & Cobbold (1992), Leever et al. (2011a) described a 3-stage evolution of the strain field during transpression from distributed strain to full partitioning.

Expanding the work of these authors, we describe the progression observed in our models (Figure 6) by combining wrench tectonics within the wedge (e.g., Naylor et al., 1986; Tchalenko, 1970; Wilcox et al., 1973) with the evolution described by Leever et al. (2011a).

Beginning with stage 1, following the period of distributed strain, strike-slip deformation is first accommodated along *R*-shear structures, as the principal infinitesimal strain axes are horizontal in wrench-dominated transpression (Tikoff & Teyssier, 1994). In stage 2, a slow-growing thrust forms on both sides of the VD eventually resulting in a bivergent wedge (30% shortening in presented models). The complete formation of thrust structures bounding the material packages provides pervasive discontinuities in the system where oblique motion preferentially concentrates. The system then enters stage 3, a transitional stage (40% shortening in presented models), where low-angle structures (<17º to the VD) and splay faults form, grow, and eventually link (see Naylor et al., 1986 for discussion). Stage 4 begins when a VD-parallel anastomosing "master fault" zone becomes apparent. Synchronously the zones of extension and principal shear narrow over the VD (70% and 100% shortening in high and low erosion models, respectively). Subsequent deformations are mostly independent, and bivergent thrusts now have a purely VD perpendicular dip-slip component while the master fault system fully accommodates the strike-slip component of bulk strain.

We observe the above stages of strain evolution across all the presented models (Figure 6). However, the difference in shortening between when the high and low erosion models enter stage 4 suggests that strain partitioning is also dependent on the erosion/rainfall rate relative to the convergence rate. By 71% shortening in the high erosion model, a VD-parallel master fault system is evident (Figure 4b, c) with high strike-slip partitioning (Figure 6). In the low erosion model, while there is an indication that these paired features are developing, the structure is geometrically and kinematically immature – in the context of a fully connected anastomosing master fault zone with localized strike-slip deformation. Considering a fully partitioned fault a continuous band of $> 1.5\ \hat{\varepsilon}_s$, for the dry model, the VD parallel strike-slip system is well-formed by 100% shortening with $\hat{\varepsilon}_s > 1.5$, yet there is also $> 1.5\ \hat{\varepsilon}_s$ on the back thrust.

The development of shear zones in the high erosion model coincides with the development of an axial valley. This observation suggests that the accelerated progression of the model through the stages of strain partitioning is linked to the erosion of fault scarps and incision by structurally controlled drainages. Therefore, feedback between the evolving stream and fault networks may accelerate strain partitioning in more erosive systems. The entrainment of streams by major faults leads to preferential incision along these structures and a positive interference with *Y*-shear formation through drainage capture, ultimately leading to the earlier appearance of a fully partitioned master wrench fault. This series is shown in Figure 4c by the increase in the 0º–15º bin and in Figure 5b by the incision of a VD parallel drainage along the trace of the master fault and capture of the headwaters of adjacent streams.

We identify two potential explanations for the earlier formation of a VD-parallel valley and earlier strike-slip partitioning: 1) focused mass removal by incision changing the stress balance in the material, thus exposing and localizing deformation earlier along actively developing *Y*- and *P*-shears, and 2) weakening of the fault by infiltration and water-induced friction reduction. However, since faults are unconfined, there should be no substantial increase in fluid pressure that would promote failure.

Considering the first mechanism, a simple analysis of the stress on the wedge-bounding thrusts and strike-slip faults shows how reducing the overburden on the wedge decreases the strength of each fault. Given a simple wedge geometry, the force normal to the thrust, F_{thrust}, is diminished by $mgcos(\theta)$, where m is the mass of the removed material, g is the acceleration due to gravity, and θ is the dip of the thrust. Correspondingly, the force normal to a VD-parallel strike-slip fault, $F_{strike\text{-}slip}$, is reduced by $mgcos(\theta)sin(\theta)$. The normal stress change, $\Delta\sigma_n$, is each force value over the fault area.

To estimate the unclamping effect caused by negative $\Delta\sigma_n$ for the presented models, we must first calculate the volume of eroded material. To do so and capture variable incision patterns in each wedge we create 5 cm wide swath profiles for the wet models at 70% shortening, with a centerline across the midsection of the innermost rhomboidal package in both models. We then integrate the difference in maximum and minimum elevations across the length of the profile to calculate the volume of eroded material. Using the density of CMII from Reitano et al. (2020), we calculate its mass. For the strike-slip fault, we estimate A given a 5 cm long fault with the height of the maximum average swath elevation. Alternatively, we estimate the A of the thrust fault as a 5 cm long patch dipping 35º. For the friction coefficient, μ, we use the wet (20 wt. % H_2O) values for CMII from Reitano et al. (2020). With these values, we estimate $\Delta\sigma_n$ on the thrust faults as ~141 Pa and ~105 Pa and the $\Delta\sigma_n$ on the strike-slip faults as 69 Pa and 51 Pa for the high and low erosion cases, respectively.

It is helpful to put $\Delta\sigma_n$ estimates into the context of the range of stresses in the wedge. For this effort, we assume a Mohr-Coulomb failure criterion (Coulomb, 1776; Mohr, 1900) and Andersonian principal stress orientations for thrust and strike-slip faults (Anderson, 1905). Given these assumptions, we estimate the normal stress on the thrust fault imposed by the mass of an equally long wedge-shaped package as ~1.9 KPa and ~0.9 KPa for a strike-slip fault striking 20º from the greatest principal stress direction. Therefore, compared to a dry scenario, erosion results in an overall "unclamping" effect on both faults by 7%-8%. There is a difference of ~2% between high and low erosion cases. Since the initial slip style of the wedge-bounding thrusts are initially oblique, the reduction in vertical stress by erosion also assists in the rotation of the stress field so that the least principal stress is vertical, and the fault behaves as purely dip slip. The different stress states in the dry versus wet cases are exemplified by the notion that the models with erosion reach a steady state by 70% shortening, yet the dry case does not until perhaps after 100% shortening (Figure 7).

4.3 Coupling between fault and stream networks to shape topography

In an oblique collision zone, the topography of the resulting mountain belt is that of a thrust bounded wedge. Relief is generally subdued but rises abruptly into a steep backslope to the main divide, which falls steeply to the indenter forming the inboard slope (Koons et al., 1994). We observe the same general morphology in our models (Figure 3). Yet, at shorter length scales (< 5 cm), there are apparent differences between the dry, high, and low erosion models. Here we argue that these topographic variations between our models depend on this faulting-surface process feedback and its impact on strain partitioning.

The interplay between tectonic and erosional factors manifests in part as the trends we see in the lateral growth of the wedge between different models (Figures 3, 4, and 7; cf. Dahlen & Suppe, 1988; Steer et al., 2014). The high erosion model has fewer, yet wider, thrust sheets. The width of these sheets is a function of gradual thickening by syntectonic deposition of alluvium and more

519 rapid and widespread erosion, leading to the preferential propagation of the basal thrust further
520 away from the wedge and reduction of surface slope (Bonnet et al., 2007; Fillon et al., 2013;
521 Malavieille, 2010; Reitano et al., 2022; Simpson, 2006; Stockmal et al., 2007). The formation of
522 additional thrusts is also delayed due to the crustal thickening, and thus, further shortening required
523 to propagate deformation into the foreland. In contrast, the low erosion model continues to expand
524 with the formation of thrust sheets and outpaces the growth of the high erosion model.

525 In Figure 7, for the models including erosion, the relationship between surface uplift and wedge
526 propagation is well explained by the critical taper model (Dahlen, 1990). In these experiments the
527 wedge reaches a critical state by 70% shortening. At this point, material accretion is fully balanced
528 by erosion out of the wedge and the wedge ceases to grow (Hilley & Strecker, 2004; Willett, 1999).
529 The onset of a steady state condition is coincident with the appearance of a fully strike-slip
530 partitioned master fault with a component of dilation, and the establishment of a subparallel main
531 axial or *R*-shear drainage. Conversely, in the dry model, wedge growth begins to stabilize by 100%
532 shortening, yet a critical state is never fully attained. This observation suggests that the stream-
533 fault feedback is fundamental in attaining an erosional steady state condition.

534 The location and amplitude of salients and recesses in the thrust belt are also controlled by the
535 along-trend distribution of erosion (Graveleau & Dominguez, 2008; Liu et al., 2020; Marshak,
536 2004). With localized erosion, as expected where the tips of synthetic faults intersect thrust toes,
537 the wedge will be driven back to a supercritical state. At an intensified condition, the propagation
538 of the thrust belt will be locally limited at these intersections. Such interactions also help to explain
539 the relatively slow wedge growth in the high erosion model. As structurally controlled drainages
540 develop more rapidly, they concentrate sediment discharge and hamper wedge growth (Liu et al.,
541 2020). The width of a wedge in an oblique system is further affected by lateral block motion along
542 *R*- and *Y*-shears. The bookshelf-style faulting along these features generally reduces the width of
543 the wedge, linking the width of the wedge to the degree of strain partitioning.

544 The swath profiles from the high erosion model shown in Figure 7d highlight how erosion,
545 incision, and deformation modify the elevation and relief of the wedge at different shortening
546 stages. The corresponding surface uplift, rock uplift, and exhumation measurements from the
547 initial to the final stage are maximum estimates for the erosion-dominated end member. We find
548 that along the master fault-axial valley, there is 1.6-2.5 cm of rock uplift and 4-6 mm of
549 exhumation, corresponding to 1.2 – 1.9 cm of surface uplift. These estimates are reasonable when
550 transferred to natural systems. With our l^* of 1×10^{-5}, these measurements translate to 1.6-2.5 km,
551 400-600 m, and 1.2-1.9 km of rock uplift, exhumation, and surface uplift, respectively.
552 Considering these figures, exhumation in a transpressional setting is greatest where the major trunk
553 streams intersect the velocity discontinuity, which from Figure 5, is approximated by the drainage
554 divide. Thus, in thermochronometric studies, we should expect the youngest dates in these zones.

555 Our results indicate that the morphology of a transpressional wedge is linked to the systematics
556 of the potential feedback between faulting and incision. Specifically, valley orientation and shape
557 vary based on the amount of precipitation/erosion, the geometry of drainage networks, and the
558 degree and duration of strike-slip partitioning. Figure 9 synthesizes the evolution of stream and
559 fault networks, strain partitioning, and topography between high and low erosion systems. The
560 synthesized stages shown here follow an initial stage of distributed strain and correspond to the
561 strain evolution stages in section 5.2.

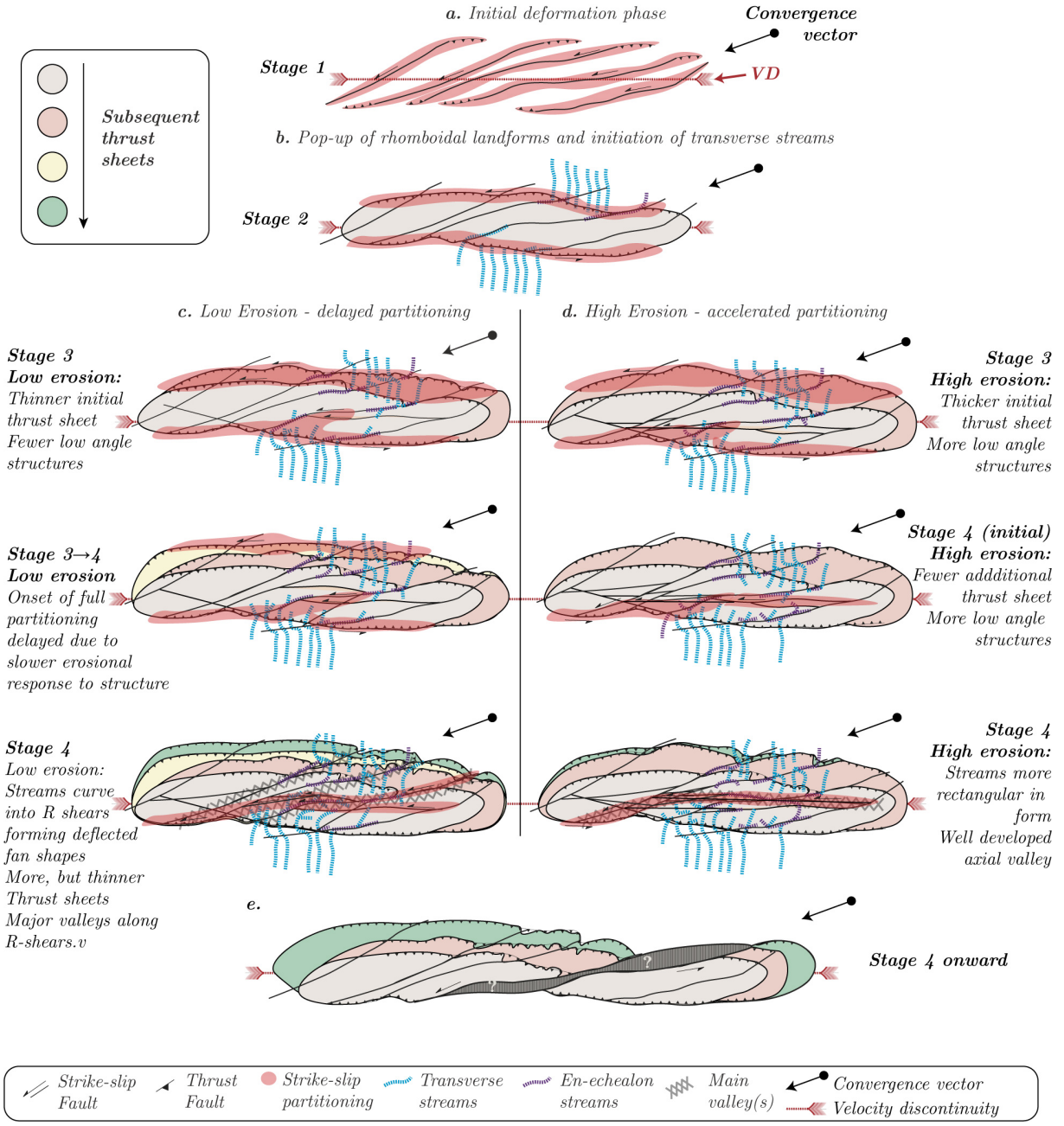

Figure 9: *Illustration highlighting the differences between the evolution of fault and stream networks, strain partitioning, and topography.* ***(a)*** *The initial deformation phase.* ***(b)*** *Beginning stages of wedge development.* ***(c)*** *Stages 3 (transitional) – 4 (full partitioning) for low erosion systems.* ***(d)*** *Stages 3 (transitional) – 4 (full partitioning) for high erosion systems.* ***(e)*** *Wedge development after full partitioning.*

Stage 1 (pre-erosion): *R*-shear structures accommodate strike-slip deformation and link laterally along thrust structures.

Stage 2: With the onset of erosion, transverse streams form along uplifted rhomboidal packages. Since wedge-bounding thrusts accommodate both the strike-slip and VD-perpendicular components of deformation, streams are mainly offset along these features.

Stage 3: A transitional phase when drainages actively respond to the progressive evolution of faults toward parallelism with underlying VD or passively rotate with simple shearing. Ridges and valleys transiently develop following the fault-stream feedback and progression toward complete partitioning. As controlled by the critical taper of the wedge, thrust sheets begin to form and propagate as a function of erosion rate and strike-slip displacement on *R-shear*s. The low erosion model has more but thinner thrust sheets. In comparison, in the high erosion scenario, a wide thrust sheet forms early on and accommodates most convergence throughout the model evolution. The high erosion model also has more low-angle strike-slip structures (*Y* and *P* shears*).* Within a radius equal to the wavelength of the dominant valleys (~5 cm), the local topography along these structures exceeds 5 mm, the highest for incised valleys in the models. These deep valleys indicate that the collocated trunk streams and shears are significant incision points. Sediment routing out of these incised valleys locally induces a supercritical state in the wedge, limiting its propagation in the near field.

Stage 4: The wedge is fully partitioned with a well-developed master fault system. The main drainage is created by stream entrainment along the master fault forming a distinct axial valley. High volumes of sediment are routed out of orogen along this valley, and exhumation is localized. This phase is reached at lower shortening in the high erosion model due to the accelerated erosion-strain partitioning feedback. The rapid evolution of strain partitioning is facilitated by heightened incision and headward erosion, more vigorous stream reorganization, and mass removal along stream networks. For streams in the low erosion model, deflection, diversion, and erosion along *R* structures lead to asymmetric forked stream networks that curve into the wedge in the direction parallel to the convergence vector. In contrast, streams in the high erosion model are more rectangular, reflecting the more prevalent capture mechanisms and the change in prevailing structures from *R* to the more VD-parallel *Y*-shears and master fault.

Post strain partitioning and wedge development: Kinematic separation of rhomboidal landforms along the master fault–main valley feature with continuous strike-slip deformation and exhumation along the master fault system.

5.1 Comparison with natural systems

Our models have numerous simplifications, including the absence of a more ductile lower crust, which we know affects strain localization (e.g., Roy & Royden, 2000a, 2000b). Moreover, because our experiments couple nonlinear deformational and topography forming processes, it is challenging to extrapolate observations made within the time frame of experimental systems or over the seismic cycle to the deformation patterns observed in large and long-lived collisional zones. While attempts have been made, there is still work to be done to fully characterize the scaling of the material transport processes and the material's deformational behavior (see section 2.1).

Concerning the boundary conditions, at depth, the VD set-up and activation of slip along the basement fault idealizes the propagation of a fault from a basement structure to an undeformed homogenous cover. Furthermore, there may be edge effects on the side of the shear zone, affecting the drainage patterns at later stages. These effects result from offsetting one side of the material package and exposing void space against the evolving orogen. Lastly, we ignore the impact of some erosional processes and modifiers, with examples including glaciation and vegetation.

Given those assumptions, the patterns in the models presented here still provide some insights into fault development and propagation, strain partitioning, dynamic river network processes, and topographic formation in transpressional orogens. There are several active or recently transpressive systems around the globe where the results of this study are relevant, some of many include the Central-Western Colombian Andes (Figure 10a; Cortés et al., 2005; Suter et al., 2008), the Merida Andes in Venezuela (Figure 10b; Audemard & Audemard, 2002; Erikson et al., 2012), and the central Transverse Ranges along the San Andres fault system (Figure 10c; Binnie et al., 2008; Blythe et al., 2002; Matti & Morton, 1993). The annual precipitation in each range varies between these orogens ranging from 200-300 $cmyr^{-1}$ in the Central–Western Colombian Andes, 50–250 $cmyr^{-1}$ in the Merida Andes, and 25 – 100 $cmyr^{-1}$ in the Central Transverse Ranges (estimated from WorldClim2, Fick & Hijmans, 2017). The key morphostructural similarities between each natural prototype and presented models are exhibited in Figure 10.

Curiously, the early-stage macroscopic topographic features we observe only exist in some of these orogens. Notably, orogen-scale repeated *R*-shear structures occur in few locations of wrench-dominated deformation (e.g., Tchalenko & Ambraseys, 1970). While these strike-slip structures are commonly observed at the micro or outcrop scale (e.g., Katz et al., 2004; Tchalenko, 1968) or in analog experiments (Burbidge & Braun, 1998; Casas et al., 2001; Naylor et al., 1986; Schreurs & Colletta, 1998; Tchalenko, 1970; Wilcox et al., 1973), the appearance of orogen-scale repeated *R-shear* structures seems to only occur in some locations of wrench dominated deformation (e.g., Tchalenko & Ambraseys, 1970). Based on experiments and natural observations, Keller et al. (1997) posit that *P* shears dominate over *R-shear*s in zones of oblique convergent deformation. The rarity of *R-shear* structures is likely linked to the varying kinematic modes of bulk strain accommodation in zones of transpressional deformation due to lithological complexity, pre-existing structural anisotropy, convergence angle, poor relief on faults or nearfield sedimentation, and climatic control.

Furthermore, as shown in experiments from the literature en-echelon, *R* features are short-lived structures considering the long-term evolution of an orogen (Wilcox et al., 1973), and thus, so is the time scale to complete strain partitioning. As follows, en-echelon strike-slip structures should be observed only in tectonically young orogeny (< 10 Myrs) with relatively consistent rheology and constant convergence angles across the zone. In other words, the global examples of transpressional tectonics only provide a snapshot of the overall evolution of a transpressional wedge. Thus, the rapid progression through the initial stages biases observations toward the final *R*-shear-absent configurations.

For the evolution and later topographic expression of transpression in nature to strongly resemble our experiments, the region must also have a nearly single-phase tectonic history with a limited amount of inherited structural anisotropy. The convergence angle also plays a significant role. At low obliquities, there is little to no strike-slip partitioning. Whereas at high obliquities, such as along the San Andreas fault system (Figure 9b), there are high degrees of strike-slip partitioning (Teyssier et al. 1995). Furthermore, salt tectonics can modify the partitioning state and lead to highly complex structures and landforms (e.g., Archer et al., 2012; Lohr et al., 2007).

The two natural prototypes that most resemble the models presented here are the Merida Andes of Venezuela and the central Transverse Ranges of the San Andreas fault system (Figure 10b, c). Though these systems are presently exposed to different climatic regimes (San Andreas – semi-Arid; Merida Andes – tropical), we focus mainly on the general results of our experiments because of other confounding variables present in natural systems (lithological heterogeneity, climatic

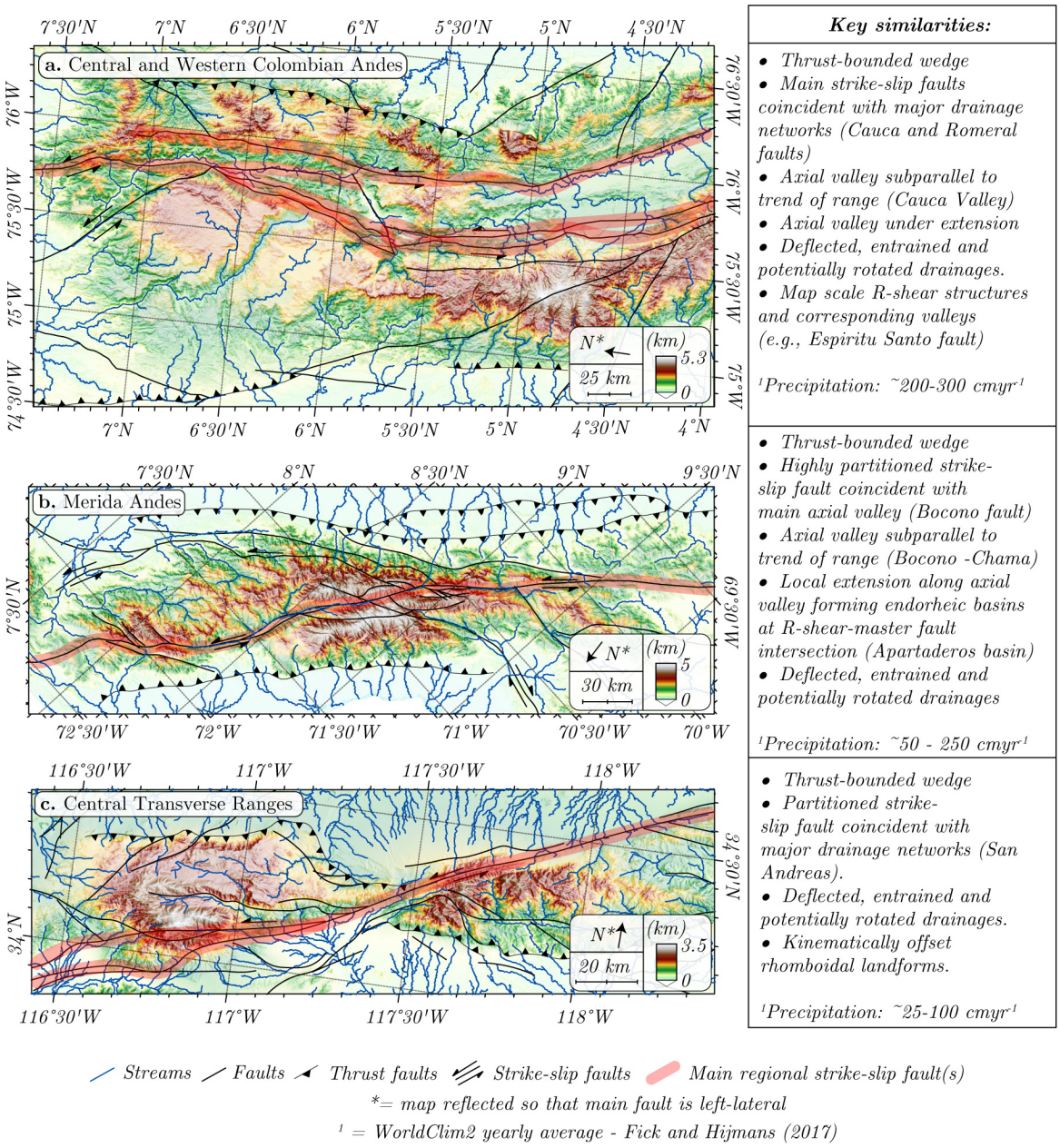

Figure 10: *Natural prototypes with similar morphostructural characteristics as our models.* ***(a)*** *The Central and Western Colombian Andes.* ***(b)*** *The Merida Andes in Venezuela.* ***(c)*** *The Central Transverse Ranges along the San Andreas Fault north of Los Angeles, California. The similarities between each setting and the models are listed in the boxes on the right of the figure. Precipitation data is derived from WorldClim2* (Fick and Hijmans, 2017)

gradients, preexisting structures). These transpressional ranges predominantly exhibit the bivergent wedge structure bounding an uplifted zone of internally deformed topography that we observe in our models.

The Merida Andes (Figure 10b) is a roughly 350 km long × 100 km wide dextral transpressional mountain range that is thought to have begun significant deformation in the Late Miocene (F. Audemard, 1992; Colletta et al., 1997; Stephan, 1982). Strike-slip deformation is highly partitioned to the Bocono fault, a 500 km dextral strike-slip system, since 15 ± 2 Ma with slip rates of 7.3 – 10.7 mm/a (Audemard, 2003). River systems in the Merida Andes exhibit similar

patterns as those described in the laboratory models, including irregular or rectangular drainages, prevalent wind gaps, beheaded or diverted rivers, and densely dissected fault scarps (Audemard, 1999). River channels exhibit deep incision with valley walls as high as 200 – 300 m (Audemard & Audemard, 2002). The high incision and active drainage reorganization result from the highly erosive setting with around 200 cm of yearly rainfall (Martin et al., 2020). The main valley cutting through the Merida Andes follows the trace of the Bocono fault, as we observe in the high erosion model. Considering the rock uplift estimates derived from our models, the trace of the Bocono fault, especially in the center of the orogen, should also correspond to the highest amounts of rock uplift and exhumation. Furthermore, the jog in the Bocono fault is appropriately aligned with the ideal *R*-shear orientation and is likely influenced by pre-existing *R*-shear structures. At the tips of the Bocono fault, large alluvial fans reflect its role in sediment routing from the internal portion of the orogen. The ~160 km long by ~40 km wide triangular feature visible in the northwestern part of the Merida Andes is likely formed by the intersection of the master fault with *R* and *P* shear structures. These similarities with model results suggest that the Merida Andes is in stage 4 (Figure 9) of the development of the transpressional system. At this point, deformation and exhumation may be localized to the Bocono fault system by the stream fault feedback. Additionally, pull apart basins present along this structure (Audemard and Audemard, 2002) express the concentrated extension we note in erosion model $\hat{\varepsilon}_m$ maps. Projecting into the future, we expect the rhomboidal landforms cut by the Bocono fault to offset left-laterally, as in Figure 9e.

The central Transverse Ranges of the San Andreas fault system (Figure 10b) are composed of two distinct lenticular mountain ranges, the San Gabriel and San Bernadino mountains, separated by the main strand of the San Andreas fault. Both mountain ranges are roughly 35 km wide and 100 km long. Beginning with the activation of the San Gabriel fault around 12 Ma, which presently bounds the San Gabriel mountains to the south, the transverse ranges were uplifted to elevations > 2000 m and vastly reconfigured. The San Bernadino block was translated as much as 200 km to the southwest by motion along the main San Andreas fault strand starting as early as 5 Ma (Blythe et al., 2002; Matti & Morton, 1993). The evolution of the Transverse ranges strongly resembles the presented model for the topographic and deformational development of transpressional wedges with the present configuration beyond stage 4 (Figure 9e).

Considering model observations, valleys corresponding to the master fault system should be the locus of exhumation in transpressional ranges (Figure 8). Where erosion/denudation estimates are available, the presented natural prototypes support this claim. In the central Transverse ranges (Figure 10b), low-temperature thermochronometric ages (Buscher & Spotila, 2007) and denudation rates from radionuclide dating (Binnie et al., 2008) support the hypothesized trends with erosion/denudation rates increasing toward the main San Andreas fault strand. The same trends are apparent further to the northwest in the San Emigdio and Mount Pinos regions, where the western Transverse ranges accommodate most transpressional deformation. There, a low-temperature north-south thermochronometric transect shows a substantial decrease in thermochronometric dates from 19.4 ± 2.4 Ma to 4.4 ± 0.7 Ma across ~10 km. The youngest dates are at higher elevations than the older dates within a hanging stream valley, similar to that observed in our models (Niemi et al., 2013). In the Merida Andes (Figure 10a), though only higher temperature $^{40}Ar/^{39}Ar$ thermochronometric data are available, the youngest Muscovite dates (approximately 135 – 200 Ma) lie along the Bocono fault on the edges of the Chama valley near the city of Mérida. Muscovite $^{40}Ar/^{39}Ar$ dates are older outside this valley at around 250 – 425 Ma (van der Lelij et al., 2016). Cosmogenic radionuclide dating (Ott et al., 2023) and low-temperature thermochronology (Pérez-Consuegra et al., 2022) from the central and western Colombian Andes

(Figure 10c) show the highest erosion/denudation rates in the lofted Cauca valley (1 km elevation) along the Romeral-Cauca fault systems. Though perhaps coincidentally, we note that the trend of the main valley in each natural prototype supports the observed differences between the final configurations of the presented high and low erosion models. In the more arid central Transverse Ranges, the wedge trend and main valley trend are dissimilar. Meanwhile, in the wetter Central-Wester Colombian Andes and Merida Andes the main valley – strike-slip feature is subparallel to the wedge trend.

5 Conclusions

Erosion plays a significant role in the morphostructural evolution of transpressional systems. High erosion models are characterized by more rectangular drainages and the earlier appearance of low-angle (*Y*- and *P*-shear) structures. In the final stage, a highly partitioned master fault and velocity discontinuity parallel (VD) axial valley form. Conversely, low erosion models have drainage networks in the form of deflected fans. Their structural evolution progresses more slowly with the protracted formation of a fully partitioned shear zone. Morphologically, major valleys in the wedge instead follow the traces of synthetic *R*-shears. We propose that these differences are the result of a feedback between stream and fault network development. With more erosion, this feedback is augmented as drainages rearrange more vigorously and incise incipient and actively evolving structures. Mass removal by incision leads to an adjustment in wedge stresses and accelerated structural reconfigurations which accommodate greater portions of the wrench component of deformation.

The results of our experiments assist in understanding patterns of rock and surface uplift and exhumation in natural transpressional systems. The proposed feedbacks between incision and strike-slip strain localization suggest that, in nature, deeply incised valleys should form along the master fault. The location of this valley is influenced by the concentration of erosion energy due to crustal weakening along fault strike. Maximum rock uplift occurs along the wedge axis, which roughly aligns with the VD. Therefore, neglecting confounding variables, including lithology, and pre-existing structure, the intersection of the VD with the throughgoing master fault–main valley feature should be the location of the maximum amount of exhumation throughout the wedge. The Merida Andes, Transverse Ranges, and central-western Colombian Andes each show patterns demonstrating this trend.

We demonstrate that fault and drainage network development are linked to deformation and exhumation patterns in a transpressional system. However, work must be done to fully understand the complexities of the stream-fault feedback, including additional analog, numerical, and field studies. Numerical models that pair the thermomechanical evolution of the wedge with surface processes would be beneficial to clarify the physics of the system and more deeply explore the parameter space. Additionally, continued tectonic-geomorphic field studies focused on continental transpressional would provide the data necessary to interpret model results more rigorously in the context of natural systems.

Acknowledgments

The authors thank F. Funicello and F. Corbi for coordinating the laboratory component of this work and granting open access to the LET lab at Roma TRE. At Roma TRE, our interpretations of lab results were enhanced through discussions with R. Lanari, R. Clementucci, P. Ballato, and G. Schmidt. The authors also thank the GFZ Helmholtz Centre Potsdam for hosting E. Conrad as a

visiting researcher during the Summer of 2022. During this time, the manuscript was greatly improved by discussions with researchers at GFZ, including O. Onken, E. Kolari, and M. Rosenthau. This visiting scholarship was funded by the German Academic Exchange Service (DAAD) short-term research grant program. TWB was partially supported by NSF EAR 1927216 and 1925939. CF was partially supported by Dipartimento di Eccellenza grant from Ministero dell'Istruzione e del Merito and from PRIN 2017-2022.

Open Research

Digital elevation models, images used for particle image velocimetry analysis, and grid files of velocity field are available for download from the Texas Data Repository (Conrad, 2023)

References:

Anderson, E. M. (1905). The dynamics of faulting. *Transactions of the Edinburgh Geological Society*, *8*(3), 387–402. https://doi.org/10.1144/transed.8.3.387

Archer, S. G., Alsop, G. I., Hartley, A. J., Grant, N. T., & Hodgkinson, R. (2012). Salt tectonics, sediments and prospectivity: an introduction. *Geological Society, London, Special Publications*, *363*(1), 1–6. https://doi.org/10.1144/SP363.1

Audemard, F. (1999). Morpho-Structural Expression of Active Thrust Fault Systems in the Humid Tropical Foothills of Colombia and Venezuela. *Zeitschrift Für Geomorphologie*, *118*, 1–18.

Audemard, F. E., & Audemard, F. A. (2002). Structure of the Mérida Andes, Venezuela: relations with the South America–Caribbean geodynamic interaction. *Tectonophysics*, *345*(1–4), 1–26. https://doi.org/10.1016/S0040-1951(01)00218-9

Audemard M., F. (1992). *Tectonics of western Venezuela* (Thesis). Rice University. Retrieved from https://scholarship.rice.edu/handle/1911/16556

Audemard M, F. A. (2003). Geomorphic and geologic evidence of ongoing uplift and deformation in the Mérida Andes, Venezuela. *Quaternary International*, *101–102*, 43–65. https://doi.org/10.1016/S1040-6182(02)00128-3

Barcos, L., Díaz-Azpiroz, M., Balanyá, J. C., Expósito, I., Jiménez-Bonilla, A., & Faccenna, C. (2016). Analogue modelling of inclined, brittle–ductile transpression: Testing analytical

models through natural shear zones (external Betics). *Tectonophysics*, *682*, 169–185. https://doi.org/10.1016/j.tecto.2016.05.021

Binnie, S. A., Phillips, W. M., Summerfield, M. A., Fifield, L. K., & Spotila, J. A. (2008). Patterns of denudation through time in the San Bernardino Mountains, California: Implications for early-stage orogenesis. *Earth and Planetary Science Letters*, *276*(1), 62–72. https://doi.org/10.1016/j.epsl.2008.09.008

Bishop, P. (1995). Drainage rearrangement by river capture, beheading and diversion. *Progress in Physical Geography: Earth and Environment*, *19*(4), 449–473. https://doi.org/10.1177/030913339501900402

Bloom, A. L. (1998). *Geomorphology: a systematic analysis of late Cenozoic landforms*. Prentice Hall Upper Saddle River.

Blythe, A. E., House, M. A., & Spotila, J. A. (2002). Low-temperature thermochronology of the San Gabriel and San Bernardino Mountains, southern California: Constraining structural evolution. In A. Barth, *Contributions to Crustal Evolution of the Southwestern United States*. Geological Society of America. https://doi.org/10.1130/0-8137-2365-5.231

Bonnet, C., Malavieille, J., & Mosar, J. (2007). Interactions between tectonics, erosion, and sedimentation during the recent evolution of the Alpine orogen: Analogue modeling insights. *Tectonics*, *26*(6). https://doi.org/10.1029/2006TC002048

Bonnet, C., Malavieille, J., & Mosar, J. (2008). Surface processes versus kinematics of thrust belts: impact on rates of erosion, sedimentation, and exhumation – Insights from analogue models. *Bulletin de La Société Géologique de France*, *179*(3), 297–314. https://doi.org/10.2113/gssgfbull.179.3.297

Burbank, D. W., & Anderson, R. S. (2011). *Tectonic Geomorphology*. John Wiley & Sons.

802 Burbidge, D. R., & Braun, J. (1998). Analogue models of obliquely convergent continental plate
803 boundaries. *Journal of Geophysical Research: Solid Earth*, *103*(B7), 15221–15237.
804 https://doi.org/10.1029/98JB00751
805 Buscher, J. T., & Spotila, J. A. (2007). Near-field response to transpression along the southern
806 San Andreas fault, based on exhumation of the northern San Gabriel Mountains, southern
807 California. *Tectonics*, *26*(5). https://doi.org/10.1029/2006TC002017
808 Casas, A. M., Gapais, D., Nalpas, T., Besnard, K., & Román-Berdiel, T. (2001). Analogue
809 models of transpressive systems. *Journal of Structural Geology*, *23*(5), 733–743.
810 https://doi.org/10.1016/S0191-8141(00)00153-X
811 Castelltort, S., Goren, L., Willett, S. D., Champagnac, J.-D., Herman, F., & Braun, J. (2012).
812 River drainage patterns in the New Zealand Alps primarily controlled by plate tectonic
813 strain. *Nature Geoscience*, *5*(10), 744–748. https://doi.org/10.1038/ngeo1582
814 Chorley, R. J., Schumm, S. A., & Sugden, D. E. (1984). *Geomorphology*. London: Routledge.
815 https://doi.org/10.4324/9780429273636
816 Cloos, H. (1928). Experimente zur inneren tektonik: Centralblatt fur Mineralogie, Abt. B.
817 Cochran, W. J., Spotila, J. A., Prince, P. S., & McAleer, R. J. (2017). Rapid exhumation of
818 Cretaceous arc-rocks along the Blue Mountains restraining bend of the Enriquillo-
819 Plantain Garden fault, Jamaica, using thermochronometry from multiple closure systems.
820 *Tectonophysics*, *721*, 292–309. https://doi.org/10.1016/j.tecto.2017.09.021
821 Colletta, B., Roure, F., de Toni, B., Loureiro, D., Passalacqua, H., & Gou, Y. (1997). Tectonic
822 inheritance, crustal architecture, and contrasting structural styles in the Venezuela Andes.
823 *Tectonics*, *16*(5), 777–794. https://doi.org/10.1029/97TC01659

824 Conrad, E. (2023). Data for: "Morpho-tectonics of Transpressional Systems: insights from
825 analog modeling." Texas Data Repository. https://doi.org/10.18738/T8/5ZKWPI
826 Conrad, E. M., Tisato, N., Di Toro, G., Carpenter, B. M., & Faccenna, C. (2020). New data on
827 the stick-slip mechanics of seismogenic faults from rotary shear experiments. In *AGU*
828 *Fall Meeting Abstracts* (Vol. 2020, pp. MR015-0011).
829 Conrad, E. M., Tisato, N., Carpenter, B. M., & Di Toro, G. (2023). Influence of Frictional Melt
830 on the Seismic Cycle: Insights From Experiments on Rock Analog Material. *Journal of*
831 *Geophysical Research: Solid Earth*, *128*(1), e2022JB025695.
832 https://doi.org/10.1029/2022JB025695
833 Cortés, M., Angelier, J., & Colletta, B. (2005). Paleostress evolution of the northern Andes
834 (Eastern Cordillera of Colombia): Implications on plate kinematics of the South
835 Caribbean region. *Tectonics*, *24*(1). https://doi.org/10.1029/2003TC001551
836 Coulomb, C. A. (1776). Essai Sur Une Application Des Maximis et Minimis a Queques
837 problems Des Statique Relatifsa1‟ Architecture. *Nem. Div. Sav. Acad, Sci*, *7*.
838 Cruz, L., Fayon, A., Teyssier, C., & Weber, J. (2007). Exhumation and deformation processes in
839 transpressional orogens: The Venezuelan Paria Península, SE Caribbean–South American
840 plate boundary. In *Special Paper 434: Exhumation Associated with Continental Strike-*
841 *Slip Fault Systems* (Vol. 434, pp. 149–165). Geological Society of America.
842 https://doi.org/10.1130/2007.2434(08)
843 Dahlen, F. A. (1990). Critical Taper Model of Fold-and-Thrust Belts and Accretionary Wedges.
844 *Annual Review of Earth and Planetary Sciences*, *18*(1), 55–99.
845 https://doi.org/10.1146/annurev.ea.18.050190.000415

Dahlen, F. A., & Suppe, J. (1988). Mechanics, growth, and erosion of mountain belts. In *Geological Society of America Special Papers* (Vol. 218, pp. 161–178). Geological Society of America. https://doi.org/10.1130/SPE218-p161

Erikson, J. P., Kelley, S. A., Osmolovsky, P., & Verosub, K. L. (2012). Linked basin sedimentation and orogenic uplift: The Neogene Barinas basin sediments derived from the Venezuelan Andes. *Journal of South American Earth Sciences*, *39*, 138–156. https://doi.org/10.1016/j.jsames.2012.04.002

Fick, S. E., & Hijmans, R. J. (2017). WorldClim 2: new 1-km spatial resolution climate surfaces for global land areas. *International Journal of Climatology*, *37*(12), 4302–4315. https://doi.org/10.1002/joc.5086

Fillon, C., Huismans, R. S., & van der Beek, P. (2013). Syntectonic sedimentation effects on the growth of fold-and-thrust belts. *Geology*, *41*(1), 83–86. https://doi.org/10.1130/G33531.1

Goren, L., Castelltort, S., & Klinger, Y. (2015). Modes and rates of horizontal deformation from rotated river basins: Application to the Dead Sea fault system in Lebanon. *Geology*, *43*(9), 843–846. https://doi.org/10.1130/G36841.1

Graveleau, F., Hurtrez, J.-E., Dominguez, S., & Malavieille, J. (2011). A new experimental material for modeling relief dynamics and interactions between tectonics and surface processes. *Tectonophysics*, *513*(1–4), 68–87. https://doi.org/10.1016/j.tecto.2011.09.029

Graveleau, F., & Dominguez, S. (2008). Analogue modelling of the interaction between tectonics, erosion and sedimentation in foreland thrust belts. *Comptes Rendus Geoscience*, *340*(5), 324–333. https://doi.org/10.1016/j.crte.2008.01.005

867 Graveleau, F., Malavieille, J., & Dominguez, S. (2012). Experimental modelling of orogenic
868 wedges: A review. *Tectonophysics*, *538–540*, 1–66.
869 https://doi.org/10.1016/j.tecto.2012.01.027
870 Graveleau, F., Strak, V., Dominguez, S., Malavieille, J., Chatton, M., Manighetti, I., & Petit, C.
871 (2015). Experimental modelling of tectonics–erosion–sedimentation interactions in
872 compressional, extensional, and strike–slip settings. *Geomorphology*, *244*, 146–168.
873 https://doi.org/10.1016/j.geomorph.2015.02.011
874 Guerit, L., Dominguez, S., Malavieille, J., & Castelltort, S. (2016). Deformation of an
875 experimental drainage network in oblique collision. *Tectonophysics*, *693*, 210–222.
876 https://doi.org/10.1016/j.tecto.2016.04.016
877 Guerit, L., Goren, L., Dominguez, S., Malavieille, J., & Castelltort, S. (2018). Landscape 'stress'
878 and reorganization from χ-maps: Insights from experimental drainage networks in
879 oblique collision setting. *Earth Surface Processes and Landforms*, *43*(15), 3152–3163.
880 https://doi.org/10.1002/esp.4477
881 Hallet, B., & Molnar, P. (2001). Distorted drainage basins as markers of crustal strain east of the
882 Himalaya. *Journal of Geophysical Research: Solid Earth*, *106*(B7), 13697–13709.
883 https://doi.org/10.1029/2000JB900335
884 Hilley, G. E., & Strecker, M. R. (2004). Steady state erosion of critical Coulomb wedges with
885 applications to Taiwan and the Himalaya. *Journal of Geophysical Research: Solid Earth*,
886 *109*(B1). https://doi.org/10.1029/2002JB002284
887 Hubbert, M. K. (1937). Theory of scale models as applied to the study of geologic structures.
888 *GSA Bulletin*, *48*(10), 1459–1520. https://doi.org/10.1130/GSAB-48-1459

Hubbert, M. K. (1951). Mechanical basis for certain familiar geologic structures. *GSA Bulletin*, *62*(4), 355–372. https://doi.org/10.1130/0016-7606(1951)62[355:MBFCFG]2.0.CO;2

Katz, Y., Weinberger, R., & Aydin, A. (2004). Geometry and kinematic evolution of Riedel shear structures, Capitol Reef National Park, Utah. *Journal of Structural Geology*, *26*(3), 491–501. https://doi.org/10.1016/j.jsg.2003.08.003

Keller, J. V. A., Hall, S. H., & McClay, K. R. (1997). Shear fracture pattern and microstructural evolution in transpressional fault zones from field and laboratory studies. *Journal of Structural Geology*, *19*(9), 1173–1187. https://doi.org/10.1016/S0191-8141(97)00042-4

Konstantinovskaia, E., & Malavieille, J. (2005). Erosion and exhumation in accretionary orogens: Experimental and geological approaches. *Geochemistry, Geophysics, Geosystems*, *6*(2). https://doi.org/10.1029/2004GC000794

Koons, P. O. (1995). Modeling the Topographic Evolution of Collisional Belts. *Annual Review of Earth and Planetary Sciences*, *23*(1), 375–408. https://doi.org/10.1146/annurev.ea.23.050195.002111

Koons, P. O. (1994). Three-dimensional critical wedges: Tectonics and topography in oblique collisional orogens. *Journal of Geophysical Research: Solid Earth*, *99*(B6), 12301–12315. https://doi.org/10.1029/94JB00611

Lague, D., Crave, A., & Davy, P. (2003). Laboratory experiments simulating the geomorphic response to tectonic uplift. *Journal of Geophysical Research: Solid Earth*, *108*(B1), ETG 3-1-ETG 3-20. https://doi.org/10.1029/2002JB001785

Lallemand, S. E., Schnürle, P., & Malavieille, J. (1994). Coulomb theory applied to accretionary and nonaccretionary wedges: Possible causes for tectonic erosion and/or frontal

accretion. *Journal of Geophysical Research: Solid Earth*, *99*(B6), 12033–12055. https://doi.org/10.1029/94JB00124

Leever, K. A., Gabrielsen, R. H., Faleide, J. I., & Braathen, A. (2011). A transpressional origin for the West Spitsbergen fold-and-thrust belt: Insight from analog modeling. *Tectonics*, *30*(2). https://doi.org/10.1029/2010TC002753

Leever, K. A., Gabrielsen, R. H., Sokoutis, D., & Willingshofer, E. (2011). The effect of convergence angle on the kinematic evolution of strain partitioning in transpressional brittle wedges: Insight from analog modeling and high-resolution digital image analysis: KINEMATICS OF STRAIN PARTITIONING. *Tectonics*, *30*(2), n/a-n/a. https://doi.org/10.1029/2010TC002823

van der Lelij, R., Spikings, R., & Mora, A. (2016). Thermochronology and tectonics of the Mérida Andes and the Santander Massif, NW South America. *Lithos*, *248–251*, 220–239. https://doi.org/10.1016/j.lithos.2016.01.006

Leopold, L. B., & Bull, W. B. (1979). Base Level, Aggradation, and Grade. *Proceedings of the American Philosophical Society*, *123*(3), 168–202.

Liu, Y., Tan, X., Ye, Y., Zhou, C., Lu, R., Murphy, M. A., et al. (2020). Role of erosion in creating thrust recesses in a critical-taper wedge: An example from Eastern Tibet. *Earth and Planetary Science Letters*, *540*, 116270. https://doi.org/10.1016/j.epsl.2020.116270

Lohr, T., Krawczyk, C. M., Tanner, D. C., Samiee, R., Endres, H., Oncken, O., et al. (2007). Strain partitioning due to salt: insights from interpretation of a 3D seismic data set in the NW German Basin. *Basin Research*, *19*(4), 579–597. https://doi.org/10.1111/j.1365-2117.2007.00338.x

933 Malavieille, J., Larroque, C., & Calassou, S. (1993). Experimental modelling of
934 tectonic/sedimentation relationships between forearc basin and accretionary wedge.
935 *Comptes Rendus-Academie Des Sciences Paris Serie 2*, *316*, 1131–1131.
936 Malavieille, Jacques. (2010). Impact of erosion, sedimentation, and structural heritage on the
937 structure and kinematics of orogenic wedges: Analog models and case studies. *GSA*
938 *Today*, 4–10. https://doi.org/10.1130/GSATG48A.1
939 Malavieille, Jacques, Dominguez, S., Lu, C.-Y., Chen, C.-T., & Konstantinovskaya, E. (2021).
940 Deformation partitioning in mountain belts: insights from analogue modelling
941 experiments and the Taiwan collisional orogen. *Geological Magazine*, *158*(1), 84–103.
942 https://doi.org/10.1017/S0016756819000645
943 Mao, Y., Li, Y., Yan, B., Wang, X., Jia, D., & Chen, Y. (2021). Response of Surface Erosion to
944 Crustal Shortening and its Influence on Tectonic Evolution in Fold-and-Thrust Belts:
945 Implications From Sandbox Modeling on Tectonic Geomorphology. *Tectonics*, *40*(5),
946 e2020TC006515. https://doi.org/10.1029/2020TC006515
947 Marshak, S. (2004). Salients, Recesses, Arcs, Oroclines, and SyntaxesA Review of Ideas
948 Concerning the Formation of Map-view Curves in Fold-thrust Belts, 131–156.
949 Martin, L. C. P., Blard, P.-H., Lavé, J., Jomelli, V., Charreau, J., Condom, T., et al. (2020).
950 Antarctic-like temperature variations in the Tropical Andes recorded by glaciers and
951 lakes during the last deglaciation. *Quaternary Science Reviews*, *247*, 106542.
952 https://doi.org/10.1016/j.quascirev.2020.106542
953 Matti, J. C., & Morton, D. M. (1993). Chapter 2: Paleogeographic evolution of the San Andreas
954 fault in southern California: A reconstruction based on a new cross-fault correlation. In

Geological Society of America Memoirs (Vol. 178, pp. 107–160). Geological Society of America. https://doi.org/10.1130/MEM178-p107

Mohr, O. (1900). Which circumstances determine the elastic limit and the rupture of a material? Journal of the Association of German Engineers.

Molnar, P., & England, P. (1990). Late Cenozoic uplift of mountain ranges and global climate change: chicken or egg? *Nature*, *346*(6279), 29–34. https://doi.org/10.1038/346029a0

Naylor, M. A., Mandl, G., & Supesteijn, C. H. K. (1986). Fault geometries in basement-induced wrench faulting under different initial stress states. *Journal of Structural Geology*, *8*(7), 737–752. https://doi.org/10.1016/0191-8141(86)90022-2

Niemi, N. A., Buscher, J. T., Spotila, J. A., House, M. A., & Kelley, S. A. (2013). Insights from low-temperature thermochronometry into transpressional deformation and crustal exhumation along the San Andreas fault in the western Transverse Ranges, California. *Tectonics*, *32*(6), 1602–1622. https://doi.org/10.1002/2013TC003377

Ott, R. F., Gallen, S. F., & Helman, D. (2023). *Erosion and weathering in carbonate regions reveal climatic and tectonic drivers of carbonate landscape evolution* (preprint). Physical: Landscape Evolution: modelling and field studies. https://doi.org/10.5194/egusphere-2022-1376

Paola, C., Straub, K., Mohrig, D., & Reinhardt, L. (2009). The "unreasonable effectiveness" of stratigraphic and geomorphic experiments. *Earth-Science Reviews*, *97*(1–4), 1–43. https://doi.org/10.1016/j.earscirev.2009.05.003

Pérez-Consuegra, N., Hoke, G. D., Fitzgerald, P., Mora, A., Sobel, E. R., & Glodny, J. (2022). Late Miocene–Pliocene onset of fluvial incision of the Cauca River Canyon in the Northern Andes. *GSA Bulletin*, *134*(9–10), 2453–2468. https://doi.org/10.1130/B36047.1

978 Perrin, C., Clemenzi, L., Malavieille, J., Molli, G., Taboada, A., & Dominguez, S. (2013).
979 Impact of erosion and décollements on large-scale faulting and folding in orogenic
980 wedges: analogue models and case studies. *Journal of the Geological Society*, *170*(6),
981 893–904. https://doi.org/10.1144/jgs2013-012
982 Philippon, M., & Corti, G. (2016). Obliquity along plate boundaries. *Tectonophysics*, *693*, 171–
983 182. https://doi.org/10.1016/j.tecto.2016.05.033
984 Pinet, N., & Cobbold, P. R. (1992). Experimental insights into the partitioning of motion within
985 zones of oblique subduction. *Tectonophysics*, *206*(3), 371–388.
986 https://doi.org/10.1016/0040-1951(92)90388-M
987 Raffel, M., Willert, C., Wereley, S., & Kompenhans, J. (2007). *Particle Image Velocimetry - A*
988 *Practical Guide (2nd Edition)*. Springer Verlag, Berlin, Heidelberg, New York. Retrieved
989 from http://www.springer.com
990 Ramberg, H. (1981). *Gravity, deformation, and the earth's crust: in theory, experiments, and*
991 *geological application* (2d ed). London: Academic Press. Retrieved from http://bvbr.bib-
992 bvb.de:8991/F?func=service&doc_library=BVB01&local_base=BVB01&doc_number=0
993 01368211&line_number=0001&func_code=DB_RECORDS&service_type=MEDIA
994 Ramsey, L. A., Walker, R. T., & Jackson, J. (2007). Geomorphic constraints on the active
995 tectonics of southern Taiwan. *Geophysical Journal International*, *170*(3), 1357–1372.
996 https://doi.org/10.1111/j.1365-246X.2007.03444.x
997 Reitano, R., Faccenna, C., Funiciello, F., Corbi, F., & Willett, S. D. (2020). Erosional response
998 of granular material in landscape models. *Earth Surface Dynamics*, *8*(4), 973–993.
999 https://doi.org/10.5194/esurf-8-973-2020

1000 Reitano, R., Faccenna, C., Funiciello, F., Corbi, F., Sternai, P., Willett, S., et al. (2022).
1001 Sediment Recycling and the Evolution of Analog Orogenic Wedges. *Tectonics*, *41*.
1002 https://doi.org/10.1029/2021TC006951
1003 Reitman, N. G., Klinger, Y., Briggs, R. W., & Gold, R. D. (2022). Climatic influence on the
1004 expression of strike-slip faulting. *Geology*, *51*(1), 18–22.
1005 https://doi.org/10.1130/G50393.1
1006 Riedel, W. (1929). Zur Mechanik geologischer Brucherscheinungen. *Centralblatt Für*
1007 *Mineralogie, Geologie Und Paläontologie*, *8*, 354–368.
1008 Roe, G. H., Stolar, D. B., & Willett, S. D. (2006). Response of a steady-state critical wedge
1009 orogen to changes in climate and tectonic forcing. In Sean D. Willett, N. Hovius, M. T.
1010 Brandon, & D. M. Fisher, *Tectonics, Climate, and Landscape Evolution*. Geological
1011 Society of America. https://doi.org/10.1130/2005.2398(13)
1012 Roy, M., & Royden, L. H. (2000a). Crustal rheology and faulting at strike-slip plate boundaries:
1013 1. An analytic model. *Journal of Geophysical Research: Solid Earth*, *105*(B3), 5583–
1014 5597. https://doi.org/10.1029/1999JB900339
1015 Roy, M., & Royden, L. H. (2000b). Crustal rheology and faulting at strike-slip plate boundaries:
1016 2. Effects of lower crustal flow. *Journal of Geophysical Research: Solid Earth*, *105*(B3),
1017 5599–5613. https://doi.org/10.1029/1999JB900340
1018 Sanderson, D. J., & Marchini, W. R. D. (1984). Transpression. *Journal of Structural Geology*,
1019 *6*(5), 449–458. https://doi.org/10.1016/0191-8141(84)90058-0
1020 Sapozhnikov, V. B., & Foufoula-Georgiou, E. (1996). Do the Current Landscape Evolution
1021 Models Show Self-Organized Criticality? *Water Resources Research*, *32*(4), 1109–1112.
1022 https://doi.org/10.1029/96WR00161

1023 Schreurs, G., & Colletta, B. (2002). Analogue modelling of continental transpression. *Journal of*
1024 *the Virtual Explorer*, *07*, 103–114.
1025 Schreurs, Guido, & Colletta, B. (1998). Analogue modelling of faulting in zones of continental
1026 transpression and transtension. *Geological Society, London, Special Publications*, *135*(1),
1027 59–79. https://doi.org/10.1144/GSL.SP.1998.135.01.05
1028 Schwanghart, W., & Scherler, D. (2014). Short Communication: TopoToolbox 2 – MATLAB-
1029 based software for topographic analysis and modeling in Earth surface sciences. *Earth*
1030 *Surface Dynamics*, *2*(1), 1–7. https://doi.org/10.5194/esurf-2-1-2014
1031 Simpson, G. D. H. (2006). Modelling interactions between fold–thrust belt deformation, foreland
1032 flexure and surface mass transport. *Basin Research*, *18*(2), 125–143.
1033 https://doi.org/10.1111/j.1365-2117.2006.00287.x
1034 Steer, P., Simoes, M., Cattin, R., & Shyu, J. B. H. (2014). Erosion influences the seismicity of
1035 active thrust faults. *Nature Communications*, *5*(1), 5564.
1036 https://doi.org/10.1038/ncomms6564
1037 Stephan, J.-F. (1982). *Evolution géodynamique du domaine Caraïbe Andes et chaine Caraïbe sur*
1038 *la transversale de Barquisimeto (Vénézuéla)* (PhD Thesis). Éditeur inconnu.
1039 Stockmal, G. S., Beaumont, C., Nguyen, M., & Lee, B. (2007). Mechanics of thin-skinned fold-
1040 and-thrust belts: Insights from numerical models. In *Special Paper 433: Whence the*
1041 *Mountains? Inquiries into the Evolution of Orogenic Systems: A Volume in Honor of*
1042 *Raymond A. Price* (Vol. 433, pp. 63–98). Geological Society of America.
1043 https://doi.org/10.1130/2007.2433(04)

1044 Suter, F., Sartori, M., Neuwerth, R., & Gorin, G. (2008). Structural imprints at the front of the
1045 Chocó-Panamá indenter: Field data from the North Cauca Valley Basin, Central
1046 Colombia. *Tectonophysics*, *460*(1), 134–157. https://doi.org/10.1016/j.tecto.2008.07.015
1047 Tchalenko, J. S. (1968). The evolution of kink-bands and the development of compression
1048 textures in sheared clays. *Tectonophysics*, *6*(2), 159–174. https://doi.org/10.1016/0040-
1049 1951(68)90017-6
1050 Tchalenko, J. S. (1970). Similarities between Shear Zones of Different Magnitudes. *GSA*
1051 *Bulletin*, *81*(6), 1625–1640. https://doi.org/10.1130/0016-
1052 7606(1970)81[1625:SBSZOD]2.0.CO;2
1053 Tchalenko, J. S., & Ambraseys, N. N. (1970). Structural Analysis of the Dasht-e Bayaz (Iran)
1054 Earthquake Fractures. *Geological Society of America Bulletin*, *81*(1), 41.
1055 https://doi.org/10.1130/0016-7606(1970)81[41:SAOTDB]2.0.CO;2
1056 Teyssier, C., Tikoff, B., & Markley, M. (1995). Oblique plate motion and continental tectonics.
1057 *Geology*, *23*(5), 447–450. https://doi.org/10.1130/0091-
1058 7613(1995)023<0447:OPMACT>2.3.CO;2
1059 Thielicke, W., & Sonntag, R. (2021). Particle Image Velocimetry for MATLAB: Accuracy and
1060 enhanced algorithms in PIVlab. *Journal of Open Research Software*, *9*(1), 12.
1061 https://doi.org/10.5334/jors.334
1062 Tikoff, B., & Teyssier, C. (1994). Strain modeling of displacement-field partitioning in
1063 transpressional orogens. *Journal of Structural Geology*, *16*(11), 1575–1588.
1064 https://doi.org/10.1016/0191-8141(94)90034-5
1065 Vermeer, P. A., & De Borst, R. (1984). Non-associated plasticity for soils, concrete and rock.
1066 *HERON, 29 (3), 1984*.

1067 Viaplana-Muzas, M., Babault, J., Dominguez, S., Van Den Driessche, J., & Legrand, X. (2015).
1068 Drainage network evolution and patterns of sedimentation in an experimental wedge.
1069 *Tectonophysics*, *664*, 109–124. https://doi.org/10.1016/j.tecto.2015.09.007
1070 Viaplana-Muzas, M., Babault, J., Dominguez, S., Van Den Driessche, J., & Legrand, X. (2019).
1071 Modelling of drainage dynamics influence on sediment routing system in a fold-and-
1072 thrust belt. *Basin Research*, *31*(2), 290–310. https://doi.org/10.1111/bre.12321
1073 Wessel, P., Luis, J. F., Uieda, L., Scharroo, R., Wobbe, F., Smith, W. H. F., & Tian, D. (2019).
1074 The Generic Mapping Tools Version 6. *Geochemistry, Geophysics, Geosystems*, *20*(11),
1075 5556–5564. https://doi.org/10.1029/2019GC008515
1076 Wilcox, R. E., Harding, T. P., & Seely, D. R. (1973). Basic Wrench Tectonics. *AAPG Bulletin*,
1077 *57*. https://doi.org/10.1306/819A424A-16C5-11D7-8645000102C1865D
1078 Willett, S. D. (1999). Orogeny and orography: The effects of erosion on the structure of
1079 mountain belts. *Journal of Geophysical Research: Solid Earth*, *104*(B12), 28957–28981.
1080 https://doi.org/10.1029/1999JB900248
1081 Zeitler, P. K., Koons, P. O., Bishop, M. P., Chamberlain, C. P., Craw, D., Edwards, M. A., et al.
1082 (2001). Crustal reworking at Nanga Parbat, Pakistan: Metamorphic consequences of
1083 thermal-mechanical coupling facilitated by erosion. *Tectonics*, *20*(5), 712–728.
1084 https://doi.org/10.1029/2000TC001243